J. Fluid Mech. (2022), *vol*. 942, A57, doi:10.1017/jfm.2022.406

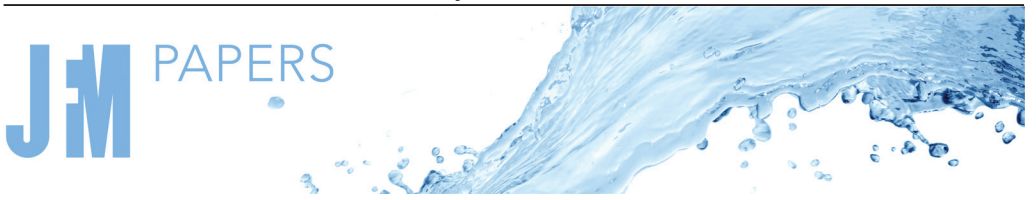

Flow-induced coupled vibrations of an elastically mounted cylinder and a detached flexible plate

Charu Mittal[1] **and Atul Sharma**[1],†

[1]Department of Mechanical Engineering, Indian Institute of Technology Bombay, Mumbai, Maharashtra 400076, India

(Received 19 July 2021; revised 3 April 2022; accepted 30 April 2022)

A fluid multi-structure interaction (FMSI) study on flow-induced coupled vibrations of an elastically mounted cylinder and a detached flexible plate is carried out numerically at a constant $Re = 100$. The effect of a non-dimensional gap G^* between the two structures, and reduced velocity U_c^*, on the proximity-induced coupled flow physics and vibration characteristics of the system is presented. The FMSI system shows a two-state response: state 1 at larger gaps $G^* \geqslant 1$, and state 2 at smaller gaps $G^* \leqslant 0.5$. At larger U_c^*, the plate encounters an oscillating wake flow in state 1, while it encounters onset of gap flow in state 2. Each state relates to distinct vibration characteristics of both the structures, with the cylinder showing a vortex-induced vibration response in state 1 and a galloping response in state 2. The amplitude response of the cylinder is governed by gap flow dynamics while that of the plate is governed by the cylinder–plate vortex-interaction dynamics. In addition to the constructive and destructive vortex interactions reported earlier, a partial vortex interaction is observed here. The vortex interactions in the near wake lead to distinct vortex-shedding patterns – 2S, C(2S), 2P and a novel C(2P) – in the far wake. Separate regime maps are presented for the various types of cylinder–plate vortex interactions and vortex-shedding patterns, correlated with the amplitude, frequency and phase difference of the coupled vibrations of the cylinder and plate. The vortex dynamics shows a strong correlation with the quantitative vibration parameters, indicating the strongly coupled multi-physics characteristics of the present FMSI system.

Key words: flow-structure interactions, vortex interactions, vortex shedding

1. Introduction

Fluid multi-structure interaction (FMSI) is an interaction of more than one movable and/or deformable structure with an external or internal fluid flow. The FMSI phenomenon is

† Email address for correspondence: atulsharma@iitb.ac.in

observed more commonly in the case of external flows, and involves a multi-physics coupling between the fluid dynamics and the structural mechanics. External flow across a body, encountered widely in nature as well as engineering applications, has been mostly studied with a canonical cylindrical structure in free-stream flow. Such a flow is often unsteady, and the associated unsteady forces lead to flow-induced vibrations (FIV). As compared to the FIV of a single structure, FMSI involves flow-induced coupled vibrations (FICV) if the spacing between the structures is small enough – called more precisely proximity-based FICV here. FIV/FICV are usually considered an undesirable phenomenon, where the vibrations may lead to the failure of the structure, such as that of the Tacoma Narrows Bridge. However, more recently, they are being utilized effectively for energy harvesting (Allen & Smits 2001; Bernitsas *et al.* 2008; Villarreal & Vortex Bladeless SL 2018).

FIV/FICV based energy harvesting is categorized into four techniques (Rostami & Armandei 2017; Wang *et al.* 2020): (i) flutter (Bae *et al.* 2014), (ii) galloping (Barrero-Gil, Alonso & Sanz-Andres 2010), (iii) vortex-induced vibration (VIV) (Bernitsas *et al.* 2008), and (iv) wake galloping/buffeting (Jung & Lee 2011). Flutter and galloping are divergent systems, where the structure oscillates with a high amplitude as the incoming fluid velocity increases. Both of these are usually low-frequency phenomena, which occur at a high cut-in speed. Unlike these divergent systems, high-amplitude VIV occurs over an intermediate range of fluid velocities. VIV results in regular structural vibrations, which are caused by a periodic vortex-shedding-based asymmetric pressure distribution. Wake galloping/buffeting occurs due to the unsteadiness in the incoming flow, which may be caused by the proximity interference of another structure or by the turbulence in the incoming flow. Although each of these techniques has its own set of advantages, the relatively low cut-in speed and the non-divergent nature of VIV and wake galloping make them favourable for energy harvesting at low fluid velocities, and they are of interest to the present work. A concise literature survey for the two techniques is presented here. The two techniques are associated with non-dimensional parameters: Re as the flow parameter; structural parameters M_c^*, ζ and U_c^* for VIV of an elastically mounted cylinder, and M_p^*, ν_s and K_b for wake galloping of a flexible plate; and G^*, L^* and t^* as the geometrical parameters. These non-dimensional parameters are presented in table 1.

VIV is discussed extensively in the review works by Sarpkaya (2004), Bearman (2011) and Williamson & Govardhan (2004), and in books by Blevins (1990) and Païdoussis, Price & De Langre (2010). It is studied most extensively for an elastically mounted (with a spring and a damper) circular cylinder, the response of which is governed by the Reynolds number Re, mass ratio M_c^*, damping ratio ζ, and reduced velocity U_c^*. The literature survey is presented here only for the VIV response at low Re. The cylinder shows a two-branch amplitude response with increasing U_c^* – initial branch and lower branch – with the transition between the branches being hysteretic (Prasanth & Mittal 2008). The branch transition is accompanied by a 180° jump in the phase difference ϕ_c, between the lift coefficient $C_L(\tau)$ and the cylinder displacement $Y_c(\tau)$. This transition is not associated with a drastic change in the vortex pattern; however, the vortex formation mode changes from 2S (two single vortices being shed per cycle) to C(2S) (coalesced vortices of similar signs, arranged in two distinct rows) and back to 2S mode with increasing U_c^* (Prasanth & Mittal 2008). The high-amplitude region in VIV falls in the lock-in regime, where the frequency f of the driving force locks on to the natural frequency of the structure (f_n), or $f^* = f/f_n \approx 1$ for large M_c^*. However, for low mass ratio, $f^* > 1$ in the lock-in regime.

Symbol	Description
	Non-dimensional parameters
Re	Reynolds number ($u_\infty D/\nu_f$)
M^*	Mass ratio (m/m_d)
ζ	Damping ratio ($c/4\pi m f_n$)
U_c^*	Reduced velocity ($u_\infty/f_n D$)
K_b	Non-dimensional bending stiffness ($Et^3/12\rho_f u_\infty^2 L^3$)
G^*	Non-dimensional gap between structures (G/D)
L^*	Non-dimensional plate length (L/D)
t^*	Non-dimensional plate thickness (t/D)
	Dimensional parameters
u_∞	Dimensional free-stream velocity
D	Diameter of the cylinder
ν_f	Kinematic viscosity of the fluid
ν_s	Poisson's ratio
E	Young's modulus of the plate
ρ_f	Density of the fluid
ρ_s	Density of the plate
L	Dimensional length of the plate
G	Dimensional gap between two structures
t	Dimensional thickness of the plate
m	Mass of the structure
m_d	Mass of the fluid displaced
c	Damping coefficient
f_n	Natural frequency

Table 1. Governing parameters for the present problem.

The maximum amplitude is limited to $A_c^* \leqslant 0.6$, with the appearance of a P+S vortex-shedding pattern (Williamson & Govardhan 2004).

The effect of the damping ratio on VIV is fairly monotonic, i.e. A_c^* decreases continuously with increasing ζ. The effect of the two parameters M_c^* and ζ was combined in the work of Griffin, Skop & Ramberg (1975) as a single mass-damping parameter ($M_c^*\zeta$) or the Skop–Griffin parameter $S_G = 2\pi^3 St_{st}^2 (M_c^*\zeta)$, where St_{st} is the vortex-shedding frequency of a stationary cylinder. The maximum amplitude attained in VIV was found to collapse on a single curve when plotted against S_G. A limiting case for the dependence of VIV on the mass of the cylinder, and the properties of the elastic mounting, was carried out by Shiels, Leonard & Roshko (2001). They reported the occurrence of large-amplitude oscillations even for a massless cylinder without spring and damper. The nature of VIV is also affected by the degrees of freedom of motion (Williamson & Jauvtis 2004), blockage (Prasanth & Mittal 2008), etc.

The VIV of a single cylinder was extended to the VIV of tandem cylinders. For VIV of a circular cylinder with a stationary upstream cylinder at $Re = 2900$ and 5900, Bokaian & Geoola (1984*b*) reported the occurrence of four kinds of dynamic response: vortex-resonance (VIV), galloping, combined vortex-resonance and galloping, and separated vortex-resonance and galloping. However, for the VIV of a cylinder with a stationary downstream cylinder, only VIV and galloping response were observed (Bokaian & Geoola 1984*a*). The type of dynamic response observed varied with the streamwise and transverse gap between the cylinders, with the galloping response at smaller gaps, and vortex resonance occurring at larger gaps. For the VIV of both the cylinders in

tandem arrangement, at $Re = 200$, $M_c^* = 2.55$ and $G^* = 0.5$, Borazjani & Sotiropoulos (2009) reported a wider lock-in regime with higher amplitudes, as compared to that for an isolated cylinder. The relative magnitude of amplitude of the upstream and downstream cylinders was found to be governed by the gap flow dynamics, which refers to passage of the shear layers of the upstream cylinder through the gap between the two cylinders. The increased amplitude with larger synchronization region, for the downstream cylinder, was also reported by Laneville & Brika (1999). The upstream cylinder, however, showed an isolated-cylinder-like behaviour, possibly due to a large gap G^* between the cylinders ($G^* = 6{-}24$). Other studies on tandem cylinders include the work of Zdravkovich (1985), Zdravkovich & Medeiros (1991), Mittal & Kumar (2001) and Papaioannou *et al.* (2008).

Besides tandem cylinders, several past studies are presented for a tandem cylinder–plate configuration. Most of these studies are carried out for a rigid plate. In an attached configuration, the splitter-plate leads to increase in recirculation length and base pressure, accompanied by a decrease in drag coefficient (Apelt, West & Szewczyk 1973; Kwon & Choi 1996). Apelt *et al.* (1973) reported that the length of the plate affects the flow characteristics significantly. Short plates ($L^* < 1$) lead to a narrower wake, with the vortex formation past the trailing edge of the plate; and long plates lead to an irregular vortex street, with the vortex formation commencing upstream of the trailing edge of the plate. Complete suppression of vortex shedding is reported for very large plate length L, with critical plate length $L_c^* = 3$ at $Re = 100$ (Kwon & Choi 1996) and $L_c^* = 5$ for $Re = 160$ (Kwon & Choi 1996) as well as $Re = 10^4$ (Roshko 1954).

For a detached rigid splitter-plate ($L^* = 24$ and $Re = 140{-}3600$), Unal & Rockwell (1988) reported two vortex-formation regimes: pre-vortex and post-vortex. The two regimes correspond to extension of the recirculation region beyond and upstream of the leading edge of the plate, respectively. Large drag suppression is observed in the pre-vortex formation regime, while the drag force is close to an isolated cylinder in the post-vortex regime (Hwang, Yang & Sun 2003). For the onset of suppression of the drag force, the critical or minimum gap G_c^* between the two structures varies as: $G_c^* = 2.7$ for $L^* = 1$ at $Re = 100$ and 160 (Hwang *et al.* 2003); $G_c^* = 2.7$, 5 and 4 for $L^* = 24$ at $Re = 142$, 785 and 36 454, respectively (Unal & Rockwell 1988); and $G_c^* = 3.35$ for $L^* = 2.71$ at $Re = 14\,500$ (Roshko 1954). Serson *et al.* (2014) studied the wake transition caused by a splitter-plate for $Re = 100$, 350, $G^* = 0{-}3$ and $L^* = 0.5$, 1. They reported significant decrease in the Strouhal number St at smaller G^*, which increased discontinuously with increasing gap G^*. They found that the Strouhal number St was predicted accurately in the post-vortex regime, and overestimated in the pre-vortex regime, with the two-dimensional study as compared to the three-dimensional study. At smaller G^*, they reported that the splitter-plate stabilizes the flow that delays its transition to three-dimensionality at high Re.

For the FIV of a flexible cantilever beam-like plate attached to a stationary cylinder, Lee & You (2013) studied the effect of the length L^* ($= 1, 2, 3$) and the stiffness K_b ($\approx 0.29{-}1.73$) of the flexible plate at $Re = 100$. They observed that the mode of oscillation showed a strong dependence on L^*, while the amplitude of vibration of the plate, A_p^*, was governed mainly by K_b. Moreover, they showed that the fluid force distribution on the plate is highly non-uniform and varies with L^*. Sahu, Furquan & Mittal (2019) studied the effect of the stiffness K_b ($\approx 0.096{-}239.65$) of the attached flexible plate at $Re = 150$ and $L^* = 3.5$. They found very low plate amplitude with first-mode oscillations for $K_b < 1.53$, and a local peak for the condition where $f \approx f_{n1}$. The amplitude

increased significantly with complex modes of oscillation for $K_b > 1.53$, with $f \approx f_{n2}$. The plate dynamics showed hysteretic jumps at mode transitions. Other studies for an attached configuration include the work of Pfister & Marquet (2020) and Shukla, Govardhan & Arakeri (2013).

For the flow past a stationary cylinder with a detached flexible splitter-plate, most of the studies are experimental and for high Re. These include the work of Allen & Smits (2001) on their set-up called the 'energy-harvesting eel', Techet, Allen & Smits (2002) for the study of multiple eels, Shi, New & Liu (2013) for a low-aspect-ratio plate, and Akaydin, Elvin & Andreopoulos (2010). There are very few studies at low Re. Wang, Zhai & Zhang (2018) studied the FIV of a detached flexible plate behind a circular cylinder at $Re = 100$ and 200. They investigated the response of the system at varying cylinder–plate gaps ($G^* = 2{-}5$), and plate stiffnesses ($K_b = 0.045{-}2.88$). They found that the plate showed first-mode oscillation for smaller gaps $G^* \leqslant 3$ at $Re = 100$, with the maximum amplitude being governed by the lock-in phenomenon ($f \approx f_{n1}$). For all the other cases, the plate oscillations showed a combination of the first and second modes, with the maximum amplitude reported at the minimum K_b.

A more complex study, for the FIV of a cylinder and an attached flexible plate, was presented by Sahu *et al.* (2019) at a constant $Re = 150$. They studied the response of the system over a varying range of values of K_b ($= 0{-}5.85$), M^* ($= 5, 10, 50$) and ζ ($= 0, 0.001, 0.01$). For low stiffness K_b of the attached plate, they found that the cylinder showed a response similar to that of an isolated cylinder, whereas with stiffer plates, the cylinder showed a three-regime response: VIV, steady and galloping. They also found that increasing M^* as well as ζ affected adversely the amplitude of oscillation of the cylinder and the plate. Another study on a similar configuration was carried out by Liang *et al.* (2018) for varying plate length ($L^* = 0{-}2.5$) at high Re ($= 7000{-}66\,000$). They reported small-amplitude VIV response for $L^* \leqslant 1.1$, and a large-amplitude galloping response for longer plates.

The above literature survey shows that there are numerous studies on VIV of a rigid cylinder and on FIV of a flexible plate behind a stationary cylinder; however, there are only a few studies on VIV of an elastically mounted cylinder with an attached flexible splitter-plate. A detached flexible splitter-plate could alter significantly the vibration characteristics, as indicated in past studies on flow over tandem structures (Zdravkovich & Medeiros 1991; Gopalkrishnan *et al.* 1994; Papaioannou *et al.* 2008), and no such study is found in the literature. Thus the present FMSI study considers FICV of an elastically mounted cylinder and a detached flexible splitter-plate in tandem arrangement. The rigid cylinder is mounted with a spring and a damper system, and the flexible plate is fixed at the leading edge and free at the trailing edge. The present FMSI system involves the FICV of the two structures, caused due to the proximity–wake interference phenomenon (Borazjani & Sotiropoulos 2009). The interference-effect-based FICV leads to passive control of the FIV of the cylinder, which is of great interest in several engineering applications and can be utilized for a needs-based engineering application.

The present study aims to address some fundamental questions. (i) What are the types of proximity-induced vibration response modes of the cylinder under the effect of the downstream flexible plate (as compared to the vortex resonance and galloping responses reported in the literature for an elastically mounted cylinder with another cylinder downstream)? (ii) What is the effect of the transversely vibrating cylinder on the vibration response of the downstream flexible plate (as compared to the response reported earlier for a flexible plate behind a stationary cylinder)? (iii) What is the role of flow in

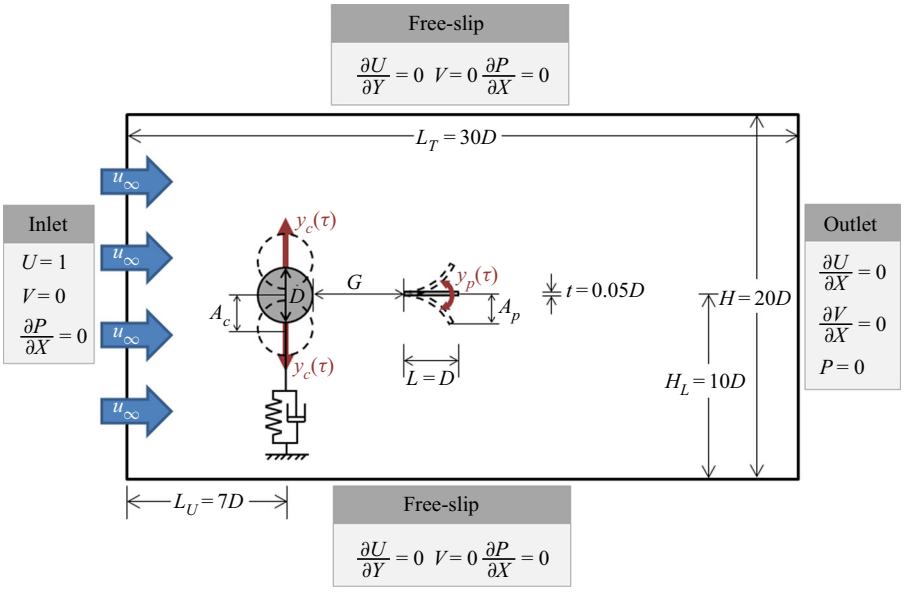

Figure 1. Computational set-up for flow-induced transverse vibration of an elastically mounted rigid cylinder and a detached flexible cantilever plate.

between the vibrating cylinder and the plate, on the coupled vibration characteristics of the two structures? (iv) What is the effect of the proximity interference on the cylinder–plate vortex interaction and the resulting vortex-shedding patterns (as compared to the 2S and C(2S) patterns reported for FIV of an isolated cylinder at low *Re*)?

2. Physical and computational set-up

The set-up for the present FMSI problem is shown in figure 1. The figure shows a free-stream flow across two structures: an elastically mounted rigid cylinder and a flexible cantilever plate. The cylinder is connected with a spring and a damper in parallel, while the plate is fixed at the leading edge and free to deform at the trailing edge. The gap G between the two structures is also shown in the figure. A periodic flow-based variation of the lift coefficient leads to a periodic displacement, represented by $Y_c(\tau)$ for the cylinder and $Y_p(\tau)$ for the trailing edge of the plate. These displacements, along with the amplitudes A_c^* and A_p^* for the respective structures, are shown in the figure. The transverse oscillations of the rigid cylinder are determined by a linear oscillator model, while the time-varying shape and kinematics of the plate are determined by the structural equations that model the fluid-dynamic force-based deformations.

Figure 1 also shows the computational domain and the non-dimensional boundary conditions for the present numerical study, with the diameter D of the cylinder and the free-stream velocity u_∞ as the length and velocity scales, respectively. Like any computational study for an external flow over a body, the length and height of the domain for the present work are constrained by the fully developed and free-slip flow conditions at the outlet and the transverse boundaries, respectively. After a domain size independence study, a domain with length $L_T = 30D$ and height $H = 20D$ is chosen, as shown in the figure.

3. Mathematical, numerical and parametric details

3.1. *Mathematical details*

The present FMSI problem involves fluid two-structure interactions. The motion of the first structure, the elastically mounted cylinder, is modelled using a linear oscillator equation, and the deformation of the second structure, the flexible plate, is modelled by considering a material that follows the Saint Venant–Kirchhoff model. The present FMSI study is modelled mathematically using the unsteady Navier–Stokes equations, the linear oscillator model, and structural equations to obtain the unsteady fluid flow, cylinder displacement and plate deformations, respectively. The fluid–structure interface dynamics are also governed by an interface boundary condition. The non-dimensional form of the governing equations and the interface boundary conditions for the present FMSI problem are given as follows.

3.1.1. *Incompressible fluid flow: Navier–Stokes equations*

$$\left.\begin{aligned} &\text{Continuity equation:} \quad \boldsymbol{\nabla}\cdot\boldsymbol{U}=0.\\ &\text{Momentum equation:} \quad \frac{\partial \boldsymbol{U}}{\partial \tau}+(\boldsymbol{U}\cdot\boldsymbol{\nabla})\,\boldsymbol{U}=-\boldsymbol{\nabla}P+\frac{1}{Re}\,\nabla^2\boldsymbol{U}. \end{aligned}\right\} \tag{3.1}$$

Here, $\boldsymbol{U}=\boldsymbol{u}/u_\infty$ is the non-dimensional fluid velocity, $P=p/\rho_f u_\infty^2$ is the non-dimensional fluid pressure, and $Re=u_\infty D/\nu$ is the Reynolds number.

3.1.2. *Elastically mounted cylinder displacement: linear oscillator model*

$$\frac{\mathrm{d}^2 Y_c}{\mathrm{d}\tau^2}+\frac{4\pi\zeta}{U_c^*}\,\frac{\mathrm{d}Y_c}{\mathrm{d}\tau}+\left(\frac{2\pi}{U_c^*}\right)^2 Y_c=\frac{2C_{L,c}}{\pi M_c^*}, \tag{3.2}$$

where Y_c is the non-dimensional transverse displacement of the cylinder, ζ is the damping ratio, U_c^* is the reduced velocity, $C_{L,c}$ is the lift force for the cylinder, and $M_c^*=4m/\pi\rho_f D^2$ is the mass ratio.

3.1.3. *Flexible-plate deformation: structural dynamics equations*

$$\left.\begin{aligned} M_p^*\,\frac{\mathrm{d}^2\boldsymbol{d}^*}{\mathrm{d}\tau^2}&=\boldsymbol{\nabla}\cdot\left(\boldsymbol{F}^*\boldsymbol{S}^*\right), \quad \boldsymbol{F^*}=I+\boldsymbol{\nabla}\boldsymbol{d}^{*\mathrm{T}},\\ \boldsymbol{S}^*&=E^*\left(\frac{2}{2(1+\nu_s)}\,\boldsymbol{G}_L^*-\frac{\nu_s}{(1+\nu_s)(1-2\nu_s)}\,\mathrm{tr}(\boldsymbol{G}_L^*)\,\boldsymbol{I}\right),\\ E^*&=E/\rho_f u_\infty^2, \quad \boldsymbol{G}_L^*=\tfrac{1}{2}\left(\boldsymbol{F}^*\boldsymbol{F}^{*\mathrm{T}}-\boldsymbol{I}\right), \end{aligned}\right\} \tag{3.3}$$

where M_p^* is the mass ratio of the plate, $\boldsymbol{d}^*$ is the non-dimensional amplitude vector, $\boldsymbol{F}^*$ is the deformation gradient tensor, $\boldsymbol{S}^*$ is the non-dimensional second Piola–Kirchhoff stress tensor, $\boldsymbol{G}_L^*$ is the Green–Lagrange strain tensor, E^* is the non-dimensional stiffness, and ν_s is Poisson's ratio.

3.1.4. *Fluid-structure interface boundary conditions:*
The velocity and the traction fields are continuous across the interface of the fluid and the structure. The interfacial boundary condition for the cylinder is given as

$$\frac{\mathrm{d}Y_c}{\mathrm{d}\tau} = \boldsymbol{U}_{f,int} \cdot \hat{\boldsymbol{j}}, \tag{3.4}$$

where $\boldsymbol{U}_{f,int}$ is the fluid velocity at the interface. The interfacial boundary conditions for the plate are given as

$$\frac{\mathrm{d}\boldsymbol{d}^*}{\mathrm{d}\tau} = \boldsymbol{U}_{f,int} \quad \text{and} \quad \boldsymbol{\sigma}_{s,int} \cdot \hat{\boldsymbol{n}} = \boldsymbol{\sigma}_{f,int} \cdot \hat{\boldsymbol{n}}, \tag{3.5a,b}$$

where $\boldsymbol{\sigma}_{s,int}$ and $\boldsymbol{\sigma}_{f,int}$ are the Cauchy stress tensor for the solid and the fluid, respectively. Here, $\hat{\boldsymbol{n}}$ is a vector normal to the interface.

3.2. *Numerical details*

A level set function-based immersed interface method (LS-IIM), which was proposed in our recent work (Thekkethil & Sharma 2019), is used for the present two-way coupled FMSI problem. The LS-IIM involves a block-iterative partitioned approach based hybrid Lagrangian–Eulerian method (Thekkethil & Sharma 2020). It uses a physical law and discrete (independent of continuous) maths-based finite volume method (Sharma 2016) for computational fluid dynamics (CFD), a geometrically non-linear Galerkin finite element method (FEM) for computational structural dynamics (CSD), and an implicit coupling between the CFD and CSD solvers. The LS-IIM uses a time-invariant non-uniform and non body-fitted Cartesian grid for the finite volume method (FVM) based flow solver, and a triangular mesh for the FEM based structural solver. A direct implementation of the fluid–solid interface boundary conditions and an implicit coupling between the solvers makes the present LS-IIM code computationally stable for large-deformation fluid–structure interaction problems involving complex geometries. For the implicit coupling, the interface variables are updated using Aitken's acceleration-method-based under-relaxation factor, after the solution of both the solvers. The updated variables are used for the next iteration of both the solvers, until convergence of residuals for the interface variables. Both the solvers are based on an implicit method, where a QUICK scheme for the advection term, along with a central difference scheme for the diffusion term, is used in the flow solver; and a generalized Newmark scheme for the time variation (Zienkiewicz, Kelly & Bettess 1977) with a second-degree polynomial approximation is used in the structural solver. An order-of-accuracy study of the LS-IIM was presented by Thekkethil & Sharma (2019), where the present method is demonstrated to be second-order accurate. The above details of the present structural solver are similar to that used recently by Sahu *et al.* (2019) for the simulation of FIV of a cylinder with an attached flexible splitter-plate.

In the present in-house solver, the fluid, solid and interface variables are first assigned with values from the initial condition (for the first time step) or the previous time step (for later time steps). Thereafter, the level set function ϕ_L is defined at each point in the Cartesian grid, using the present position of the fluid–structure interface. Then ϕ_L, along with the available flow field, is used to solve the flow solver. The obtained velocity and pressure fields are post-processed to calculate the hydrodynamic forces acting at the interface of each of the structures. Using these hydrodynamic forces as

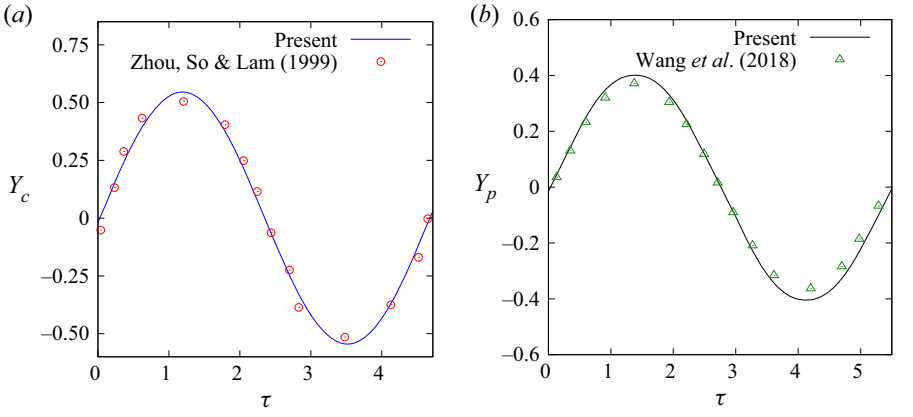

Figure 2. Validation study for free-stream flow past (*a*) an elastically mounted cylinder (at $Re = 200$, $M_c^* = 1.27$, $\zeta = 0.0034$ and $U_c^* = 3.49$), and (*b*) a detached flexible plate behind a stationary cylinder (at $Re = 200$, $L^* = 2$, $G^* = 3$, $K_b = 0.15$ and $\rho^* = 10$): temporal variation of (*a*) cylinder displacement Y_c and (*b*) plate-tip displacement Y_p, at the periodic state.

the boundary condition, the structural solver is used to obtain the deformation and velocity of each structure. The deformations and velocities are used to update the interface variables, employing Aitken's acceleration-method-based under-relaxation factor. The updated interface variables are used for the solution of the flow solver, followed by the structural solver, until convergence of residuals. The detailed solution algorithm for the present flow solver and structural solver, along with their implicit coupling, can be found in the work of Thekkethil & Sharma (2019, 2020).

3.3. *Code validation, grid independence and domain length independence studies*

The present code was validated with several benchmark cases by Thekkethil & Sharma (2019) and used in a series of fish-inspired biomimetic studies (Thekkethil, Sharma & Agrawal 2018, 2020; Gupta *et al.* 2021). Further validations of the code are presented in figure 2, with good agreement between the present and published results on periodic variation of the displacements of the cylinder Y_c (figure 2*a*) and plate-tip Y_p (figure 2*b*). Further, for the flow across a stationary cylinder with a detached flexible plate, excellent agreement between the present and published instantaneous vorticity contours is presented in our recent work (Mittal & Sharma 2021).

For the grid independence study, three different non-uniform Cartesian grids are considered: 546×363, 654×438 and 820×548, with the finest uniform grid sizes as 0.015, 0.0125 and 0.01. These are used in a rectangular region, of size $6D \times 4D$, enclosing the cylinder and plate (figure 3). For the respective grid sizes, coarsest uniform grid sizes 0.3, 0.25 and 0.2 are used far away from the structures. Hyperbolic stretching is used to generate a non-uniform grid, with a smooth transition between the coarse grid and the fine grid. For the present problem, at $G^* = 0.1$, $U_c^* = 3.3$ and $Re = 100$, the amplitudes of vibrations are $A_c^* = 0.5104, 0.5229, 0.5235$ and $A_p^* = 0.643, 0.6551, 0.6692$ for the coarsest, intermediate and finest grid sizes, respectively. The differences between the results of the coarsest and finest grids are 2.5 % for A_c^*, and 3.92 % for A_p^*. For the respective amplitudes, the differences reduce substantially to 0.11 % and 2.1 % for

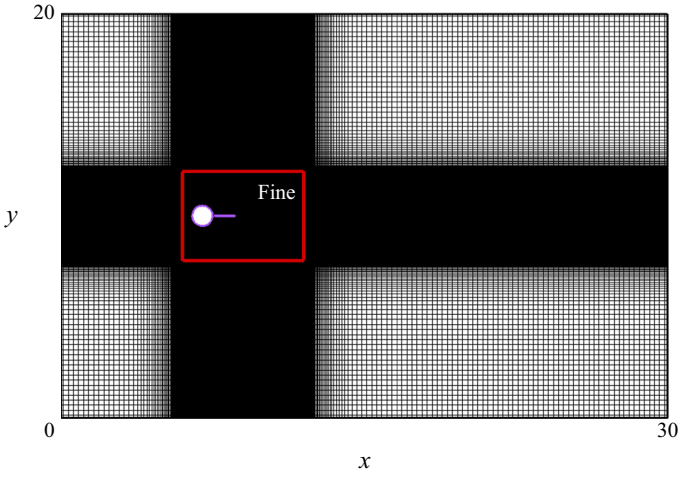

Figure 3. Non-uniform Cartesian grid of size 654 × 438, used in the fluid domain for the present work. The rectangular region, enclosing the cylinder and the plate, corresponds to a uniform fine grid size 0.0125.

the intermediate grid, with reference to the finest grid. Thus an intermediate grid size 654 × 438 is used in the present simulations.

A domain length independence study is carried out at $G^* = 0.5$ and $U_c^* = 5.5$ for three domain lengths, $L_T = 20D$, $30D$ and $40D$. For the temporal variation of the cylinder displacement $Y_c(\tau)$, the maximum variation in Y_c is found to reduce from 3.19 % for $L_T = 20D$ to 0.09 % for $L_T = 30D$, as compared to $L_T = 40D$. Thus the present simulations are carried out for $L_T = 30D$.

3.4. *Parametric details*

The scope of the present work is to study the effect of proximity of the two structures and the stiffness of elastic-mounting of the cylinder on the FMSI characteristics of the system. The respective effects are studied with the non-dimensional parameters as follows:

(i) non-dimensional gap G^*: 0.1, 0.3, 0.5, 1.0, 1.5, 2.0, 2.5; and
(ii) reduced velocity U_c^*: 1, 2, 3.3, 4, 5, 5.6, 6.7, 7.7, 10, 12.5

at constant $Re = 100$, $M_c^* = 1$, $\zeta = 0.005$, $M_p^* = 100$, $K_b = 0.21$, $\nu_s = 0.4$, $L^* = 1$ and $t^* = 0.05$. Note that the parameters associated with the cylinder and the plate are demarcated by subscripts c and p, respectively. The above values of the gap G^* are chosen such that the plate lies within as well as outside the recirculation region behind the cylinder. The other varying parameter U_c^* is a significant fluid–structure interaction parameter for VIV of a cylinder (Williamson & Govardhan 2004), which relates the time scales of the fluid and solid.

The effect of the above non-dimensional input parameters on the FMSI characteristics is quantified in terms of non-dimensional output parameters: amplitude A^*, frequency ratio f^*, lift coefficient C_L, phase difference ϕ between the temporal variation of displacement Y and the lift force C_L, and phase difference $\phi_{c,p}$ between the temporal variation of displacement of the cylinder (Y_c) and the tip of the plate (Y_p). The output parameters are given as

$$A^* = \frac{A}{D}, \quad f^* = \frac{f}{f_n}, \quad C_L = \frac{F_L}{\frac{1}{2}\rho_f u_\infty^2 D}, \tag{3.6a–c}$$

where A is the dimensional amplitude, f is the oscillation frequency, f_n is the natural frequency of vibration, and F_L is the hydrodynamic lift force per unit length. Note that the above parameters are considered separately for the cylinder (A_c^*, f_c^*, $C_{L,c}$ and ϕ_c) and plate (A_p^*, f_p^*, $C_{L,p}$ and ϕ_p), where $f_c = f_p$ for the present problem.

4. FICV characteristics: proximity-induced transition in the states of vibration response of the cylinder and the plate

FIV characteristics of a structure are represented by the amplitude and frequency of periodic vibrations. These parameters are associated closely with the relative phase of the periodically varying lift coefficient $C_L(\tau)$ and the resulting transverse displacement $Y(\tau)$ of the driven structure, expressed in terms of phase difference ϕ between the two parameters. Hence, in the present section, the coupled FIV characteristics of the cylinder as well as the plate are presented in terms of the amplitude A^*, frequency ratio f^*, and phase difference ϕ. The phase difference is calculated using a fast Fourier transform. The phase difference ϕ_p is defined as the phase difference between temporal variations of the space-averaged (not local) lift coefficient $C_{L,p}$ of the plate and the displacement Y_p of the tip of the plate. Since the plate vibrates with the first mode, for all the cases considered here, ϕ_p also corresponds to the phase of Y_p at any point along the length of the plate. Substantial variation in the vibration parameters for the present coupled FMSI system, as compared to an isolated fluid–structure interaction system, indicates a strong coupling between the FIV of the two structures.

Initially, FIV characteristics of a cylinder without the flexible plate (isolated system) are presented in § 4.1 to establish the baseline response of the system. Thereafter, for the present FMSI problem, proximity-induced two states of the amplitude response are presented separately for the cylinder and the flexible plate in §§ 4.2 and 4.3, respectively. Finally, for each of the two states of amplitude response, § 4.4 presents the amplitude A^*, frequency ratio f^* and phase difference ϕ together for the cylinder and the plate, that lead us to a comprehensive discussion on the coupled vibration characteristics of the two structures in the present FMSI system. For the few cases of non-periodic motions (obtained here for $G^* = 0.1$ at $U_c^* = 7.7{-}12.5$ and for $G^* = 0.3$ at $U_c^* = 12.5$), the maximum amplitude is presented here, similar to that reported by Leontini, Thompson & Hourigan (2006) for the VIV of an isolated cylinder. Also, for a few cases with multiple frequencies, the dominant frequency is presented.

4.1. *FIV characteristics of an elastically mounted cylinder*

The FIV characteristics of an isolated circular cylinder are shown in figure 4, where a rapid increase followed by a gradual decay trend is seen in figure 4(*a*) for the variation of the amplitude A_c^* with increasing U_c^*. Similar to the work of Sahu *et al.* (2019) on FIV of a circular cylinder at $Re = 150$, the amplitude response in figure 4(*a*) is categorized into two branches: initial branch (IB) and lower branch (LB), enveloped by a desynchronization (DS) region. This demarcation is in contrast to the three-branch (initial, upper and lower) response observed at high Re for low $M_c^*\zeta$ (Williamson & Govardhan 2004). The high-amplitude region in both of these response types is commonly marked as the lock-in regime, where the vortex-shedding frequency synchronizes with the vibration frequency. Since the basis to identify the lock-in regime is not defined uniquely in the past studies, the slope of the amplitude curve in figure 4(*a*) is used here to demarcate the present lock-in regime, shown by the shaded region. The figure shows clearly that the high-amplitude

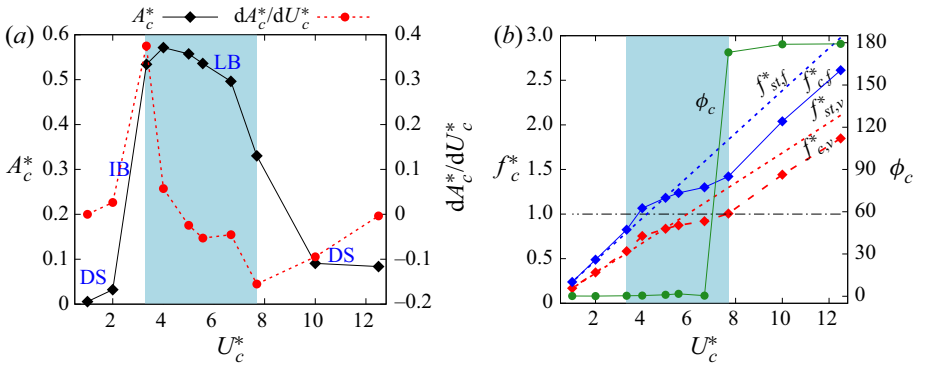

Figure 4. FIV characteristics of an isolated elastically mounted cylinder: variation of non-dimensional (*a*) cylinder amplitude A_c^*, and (*b*) frequency ratio f_c^* as well as phase difference ϕ_c (between periodic variation of lift coefficient $C_{L,c}$ and cylinder displacement Y_c), with increasing reduced velocity U_c^*, at $Re = 100$, $M_c^* = 1$ and $\zeta = 0.005$. Panel (*a*) also shows the slope of variation of A_c^* versus U_c^* that leads to the identification of the lock-in regime. Further, a demarcation of amplitude response into the initial and lower branches (IB and LB), enveloped by the desynchronization (DS) region, is presented, similar to Sahu *et al.* (2019). In (*b*), the circle symbol represents ϕ_c, while $f_{c,v}^*$ and $f_{c,f}^*$ are represented by diamond symbols.

lock-in regime is inscribed between the maximum positive/upward slope and the maximum negative/downward slope of the amplitude curve.

As stated in a review paper by Sarpkaya (1995), the frequency f of the driving force $C_{L,c}$ locks onto the natural frequency f_n of the structure in the lock-in regime. In the present case, the driving frequency f is always equal to the cylinder oscillation frequency f_c. Therefore, the frequency ratio f^*, defined as the ratio of the oscillation frequency f_c to the natural frequency $f_{n,c}$ of the cylinder, is plotted with increasing reduced velocity U_c^* as another FIV characteristic curve. At low mass ratio M_c^*, as in the present study, f_n differs significantly in vacuum and in a fluid. Hence both the natural frequency in vacuum $f_{n,v}$, as well as in fluid $f_{n,f}$, are considered for the variation of f^* as shown in figure 4(*b*). The natural frequency in the fluid is evaluated, considering the added mass m_a acting on the cylinder. The relation between $f_{n,f}$ and $f_{n,v}$ is

$$f_{n,f} = \frac{1}{2\pi}\sqrt{\frac{k}{m_c + m_a}}\,\frac{D}{u_\infty} = f_{n,v} \times \frac{1}{\sqrt{1 + \dfrac{1}{M_c^*}}} = \frac{f_{n,v}}{\sqrt{2}}. \tag{4.1}$$

With increasing U_c^*, figure 4(*b*) shows that the trend of variation of f^* is similar in vacuum as well as in fluid, closely resembling past studies (Leontini *et al.* 2006; Sahu *et al.* 2019). It can be observed that both f_f^* and f_v^* fall below the frequency ratio $f_{st}^* = f_{st}/f_n$ of a stationary cylinder at high U_c^*, indicating a smaller vortex-shedding frequency as compared to that for a stationary cylinder. Within the extent of the present lock-in regime, from $U_c^* = 3.3$ to $U_c^* = 7.7$, the shaded region in figure 4(*b*) shows a variation of f^* from $f_f^* \approx 0.82$ ($f_v^* \approx 0.58$) to $f_f^* \approx 1.42$ ($f_v^* \approx 1$). The extent of the lock-in region beyond $f_f^* \approx 1$ at the present low mass ratio M_c^* was reported in several experimental studies on VIV of a circular cylinder at high *Re* (Williamson & Govardhan 2004). However, such deviation in the lock-in region from $f_f^* \approx 1$ has not been well addressed at the low *Re* considered here. It is interesting to note that the extent of the reported high-amplitude upper branch

(obtained at large Re) within $f_f^* \approx 1$ to $f_v^* \approx 1$ (Williamson & Govardhan 2004) agrees closely with the extent of the present high-amplitude lock-in regime within $f_f^* = 0.82$ to $f_v^* = 1$ at low Re (figure 4). Leontini *et al.* (2006) also reported the extent of the lock-in regime up to $f_v^* \approx 1$ in their study on VIV of a cylinder at $Re = 200$. However, since they considered a larger mass ratio M_c^* (10 as compared to 1 here), the large difference between f_f^* and f_v^* shown in figure 4(*b*) was not evident in their study.

Figure 4(*b*) also shows the variation of the phase difference ϕ_c with increasing U_c^*. The periodic motion of the cylinder and the lift force show an in-phase ($\phi_c \approx 0^\circ$) variation up to an intermediate U_c^*, with a sharp in-phase to anti-phase ($\phi_c \approx 180^\circ$) transition with increasing U_c^*, similar to that reported earlier (Williamson & Govardhan 2004; Prasanth & Mittal 2008). It is interesting to note from figure 4(*b*) that the phase switch, from almost 0° to almost 180°, occurs at the same intermediate U_c^* where $f_{c,v}^* \approx 1$.

4.2. *Amplitude response of an elastically mounted cylinder with a flexible plate downstream*

The vibration characteristics of an isolated cylinder, presented in figure 4(*a*), indicate that the cylinder shows a rapid increase followed by a gradual decay type of amplitude response – a classic VIV curve. Introducing a flexible plate downstream to the cylinder leads to a proximity-induced coupling between the vibration of the two structures. The coupling becomes stronger with decreasing gaps G^*, leading to a proximity-induced transition in the amplitude response from the classic VIV curve at larger G^* to a rapid-increase plateau variation at smaller G^*, as shown in figure 5(*a*).

For the classic VIV response at the larger gaps $G^* \geqslant 1.0$, it is interesting to note from figure 5(*a*) that the effect of the plate on the amplitude response of the cylinder is evident mostly for the larger U_c^*, i.e. larger flexibility of the cylinder mounting. Thus, up to an intermediate $U_c^* \leqslant 4$ that almost corresponds to the lower branch, it can be seen in the figure that the peak amplitude A_c^* remains almost unchanged. For the desynchronization region at the larger U_c^*, the figure shows that the asymptotic amplitude increases with decreasing gap G^*. However, the reduction in the cylinder–plate gap to $G^* \leqslant 0.5$ leads to the transition from the VIV response to the aforementioned rapid-increase plateau amplitude response, as shown in the figure. After the transitions at smaller gaps $G^* \leqslant 0.5$, it can be seen that the proximity-induced variation in the amplitude response is evident over almost the entire range of U_c^* studied, with a slight reduction in A_c^* at smaller U_c^*, and substantial enhancement at larger U_c^*, as compared to that for an isolated cylinder. Moreover, at the larger U_c^*, the figure shows that a smaller gap G^* of the flexible plate leads to a larger proximity-induced enhancement in the cylinder amplitude A_c^*.

The present FICV study on the tandem cylinder–plate configuration is similar to FIV of the tandem cylinder–cylinder configuration. For VIV of an elastically mounted cylinder with a closely spaced elastically mounted/fixed cylinder downstream, similar amplitude responses were reported at smaller gaps G^* (Bokaian & Geoola 1984*a*; Zdravkovich & Medeiros 1991), and the present rapid-increase plateau response (figure 5*a*) was termed 'proximity-induced galloping' in the work of Bokaian & Geoola (1984*a*). Using this terminology for the present problem, figure 5(*a*) shows a transition from VIV to galloping response with decreasing gaps G^*. This transition is correlated with the flow characteristics within the gap between the transversely oscillating cylinder and the flexible plate, discussed below in § 5. Although the two amplitude responses (VIV and galloping)

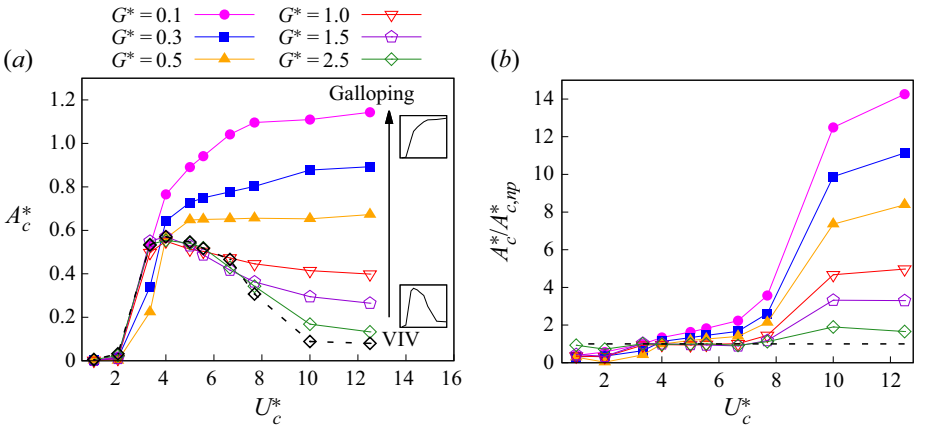

Figure 5. Effect of the non-dimensional gap G^* on the variation of (*a*) non-dimensional oscillation amplitude A_c^* of the cylinder, and (*b*) its ratio with the amplitude $A_{c,np}^*$ for the no-plate case, with increasing reduced velocity U_c^*. Panel (*a*) also shows the representative schematic for the characteristic curves of the VIV response at larger G^*, and the galloping response at smaller G^*. The respective amplitude responses are represented by unfilled and filled symbols, and the dashed line represents $A_{c,np}^*$.

observed in the present tandem cylinder–plate configuration resemble that observed earlier for the cylinder–cylinder configuration, the natures of the responses for the two systems are significantly different. At large gaps G^*, figure 5(*a*) for the present tandem cylinder–plate system shows that the magnitude and location of the peak amplitude $A_{c,max}^*$ (at $U_c^* = 4$) remain unaffected by the change in G^*. This behaviour is in contrast to the FIV of tandem cylinders, where the $A_{c,max}^*$ increases with decreasing G^*, and also shifts towards larger U_c^* (Bokaian & Geoola 1984*a*; Papaioannou *et al.* 2008). However, the widening of the high-amplitude region with decreasing gap G^* is observed for both the tandem systems. At smaller G^*, the cylinder in the present configuration shows increasing amplitude with decreasing G^*, similar to that observed for the upstream cylinder in tandem cylinders (Bokaian & Geoola 1984*a*). However, in the case of tandem cylinders, the galloping phenomenon commences at a larger U_c^* with decreasing G^* (Bokaian & Geoola 1984*a*), as compared to almost same $U_c^* = 2$ for the onset of galloping in the present tandem cylinder–plate configuration. Galloping instability was also reported by Sahu *et al.* (2019) for VIV of a cylinder with an attached flexible splitter-plate at $Re = 150$. However, they found a VIV–steady–galloping response for stiff plates ($K_b = 4.76, \infty$) and only a VIV response for highly flexible plates ($K_b = 1.75, 3.02$). As compared to their study for $G^* = 0$, the present study for varying G^* results in either VIV or galloping response of the cylinder with the flexible plate of constant stiffness ($K_b = 0.21$).

The effect of the proximity-induced coupling is demonstrated more clearly in figure 5(*b*) by the ratio of the amplitude A_c^* with plate and $A_{c,np}^*$ without plate. The figure shows that the plate causes a slight suppression in the amplitude of the cylinder for all gaps at smaller U_c^*, whereas an increase in U_c^* leads to a rapid enhancement in A_c^*. The figure also shows that the slope of the increasing amplitude ratio increases with decreasing gap G^*. The maximum amplitude enhancement factor, close to 14, is obtained here at the smallest $G^* = 0.1$ and largest $U_c^* = 12.5$. This factor occurs at a much larger U_c^* for an attached flexible plate (Sahu *et al.* 2019), as compared to the U_c^* in the present study with detached flexible plate.

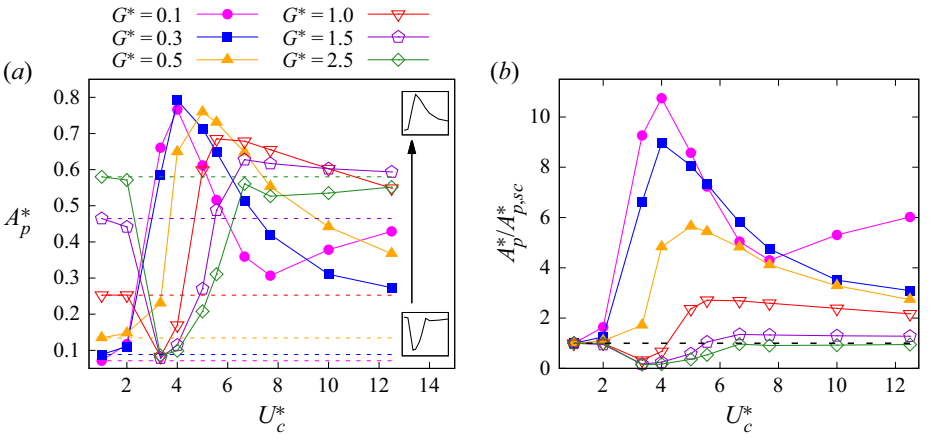

Figure 6. Effect of the non-dimensional gap G^* on the variation of (*a*) non-dimensional oscillation amplitude A_p^* of the plate, and (*b*) its ratio with the amplitude $A_{p,st}^*$ for the stationary upstream cylinder case, with increasing reduced velocity U_c^*. Panel (*a*) also shows the characteristic curves for the valley–plateau response at larger G^*, and the summit response at smaller G^*. The respective amplitude responses are represented by unfilled and filled symbols, and the dashed line represents the amplitude response $A_{p,st}^*$.

4.3. *Amplitude response of a cantilever-type flexible plate with an upstream elastically mounted cylinder*

Similar to the amplitude response A_c^* of the cylinder in figure 5(*a*), figure 6(*a*) shows two distinct amplitude responses A_p^* of the plate that occur over the same range of gaps G^* as that for the cylinder. At larger gaps $G^* \geqslant 1.0$, for which figure 5(*a*) shows the VIV response, the plate amplitude A_p^* in figure 6(*a*) shows a rapid decrease followed by a rapid increase behaviour, and finally an asymptotic variation with increasing U_c^*, i.e. a valley–plateau variation. The figure shows that at the larger G^*, the valley region commences at a smaller amplitude A_p^* and becomes narrower with decreasing gaps up to $G^* = 1.0$. The A_p^* response transforms completely at the smaller gaps $G^* \leqslant 0.5$, similar to the A_c^* response (figure 5*a*), where figure 6(*a*) shows a rapid increase followed by a gradual decay variation with increasing U_c^*, i.e. a summit curve. At smaller $G^* \leqslant 0.5$, it can be observed that the peak amplitude $A_{p,max}^*$ increases and shifts towards smaller U_c^* with decreasing G^*. Although $A_{p,max}^*$ increases with decreasing G^*, the span of the summit in figure 6(*a*) decreases and leads to a much smaller amplitude A_p^* at larger U_c^*. The plate motion loses its periodic nature at $G^* = 0.1$ for $U_c^* \geqslant 7.7$. Ignoring the non-periodic region, the figure shows a smaller G^*-based transition of plate amplitude A_p^* response from the valley–plateau curve to the summit curve. It is interesting to notice from figure 6(*a*) that the transition in the amplitude A_p^* response of the plate occurs at the same G^* ($= 0.5$) as the amplitude A_c^* response of the cylinder transitions from VIV to galloping (figure 5*a*).

Overall, figure 6(*a*) shows larger values of A_p^* over the extremities of U_c^* ($U_c^* \leqslant 2$ and $U_c^* > 7$) at the larger gaps $G^* \geqslant 1.0$, and over an intermediate range of U_c^* (2–7) at the smaller gaps $G^* \leqslant 0.5$. These amplitude variations are governed by the plate's position with respect to the recirculating region behind the cylinder and also by the interaction of the plate-tip vortex with the cylinder vortex, as presented below in § 6. Note that the plate undergoes first-mode vibrations for the various cases considered in the present work.

Higher modes are observed for a longer plate, presented in our recent work on FIV of a flexible plate in the wake of a stationary cylinder (Mittal & Sharma 2021).

The effect of proximity interference on the plate amplitude is presented further in figure 6(*b*) by the ratio of A_p^* to the plate amplitude $A_{p,st}^*$ with a stationary upstream cylinder. The figure shows that the plate amplitude ratio shows a kind of response similar to that observed in figure 6(*a*) for A_p^*. At larger gaps, the valley region corresponds to suppression in plate amplitude A_p^* due to the cylinder motion, while the plateau region results in the plate amplitude A_p^* enhancement, which increases with decreasing G^*. At smaller gaps ($G^* \leqslant 0.5$), the upstream cylinder motion enhances the plate amplitude A_p^* over the entire range of U_c^*, with the peak value at intermediate U_c^* ($\approx 4{-}5$), which increases with decreasing G^*. The maximum plate amplitude enhancement factor, close to 11, is found at the smallest $G^* = 0.1$ and an intermediate $U_c^* = 4$.

4.4. *Two states of the FICV characteristics of the cylinder as well as the plate and the associated flow regimes*

With increasing U_c^*, the amplitude responses presented above in separate subsections for the cylinder and the plate, show a proximity-induced transition at a smaller gap $G^* = 0.5$, presented schematically as insets in figures 5(*a*) and 6(*a*). Thus the present FMSI system shows two gap-based states of the coupled FIV response: state 1 at the larger gaps $G^* \geqslant 1$, and state 2 at the smaller gaps $G^* \leqslant 0.5$, shown in figure 7. Figure 7(a) shows the amplitude responses as the VIV curve for the cylinder and the valley–plateau response for the plate in state 1, whereas for state 2, figure 7(*b*) shows the response for the respective structures as the galloping variation and summit curve.

The two states of the coupled amplitude response are correlated with the ensuing wake/gap flow in between the cylinder and the plate. In state 1, the proximity-based A_c^* enhancement is observed only at the larger U_c^* ($= 7.7{-}12.5$) in figure 7(*a*). However, at $U_c^* > 7.7$, the amplitude A_c^* ($\leqslant 0.45$) is less than the radius of the cylinder. This leads to a blockage of the incidence of free-stream flow on the leading edge of the plate. Thus the flexible plate is almost subjected to an oscillating wake flow in state 1, shown schematically above figure 7(*a*). In state 2, a larger proximity-based A_c^* enhancement is observed over a broad range of U_c^* ($= 4{-}12.5$) in figure 7(*b*), and the cylinder amplitude A_c^* ($\geqslant 0.65$) is more than the radius of the cylinder. This leads to a vertical gap between the two structures (shown schematically above figure 7*b*), and a direct exposure of the plate to the free-stream flow for a certain time duration (when the cylinder displacement is $Y_c^*(\tau) > 0.5$, i.e. greater than the radius of the cylinder). This results in the onset of gap flow, as discussed in the next section. Hereafter, states 1 and 2 are referred to as oscillating wake flow and onset of gap flow, respectively. Note that the onset of gap flow seems to lead to the onset of the galloping response for the cylinder in state 2.

The effect of the two flow regimes – oscillating wake flow at larger G^* in state 1 and onset of gap flow at smaller G^* in state 2 – on the amplitude response is discussed here for decreasing G^* or increasing proximity interference between the two structures. At the larger values of U_c^*, figure 7 shows that the cylinder amplitude A_c^* increases with decreasing G^* for both flow regimes. The oscillating wake flow is associated with an increase in the plate amplitude A_p^* in state 1, while the onset of gap flow is associated with a decrease in A_p^* in state 2.

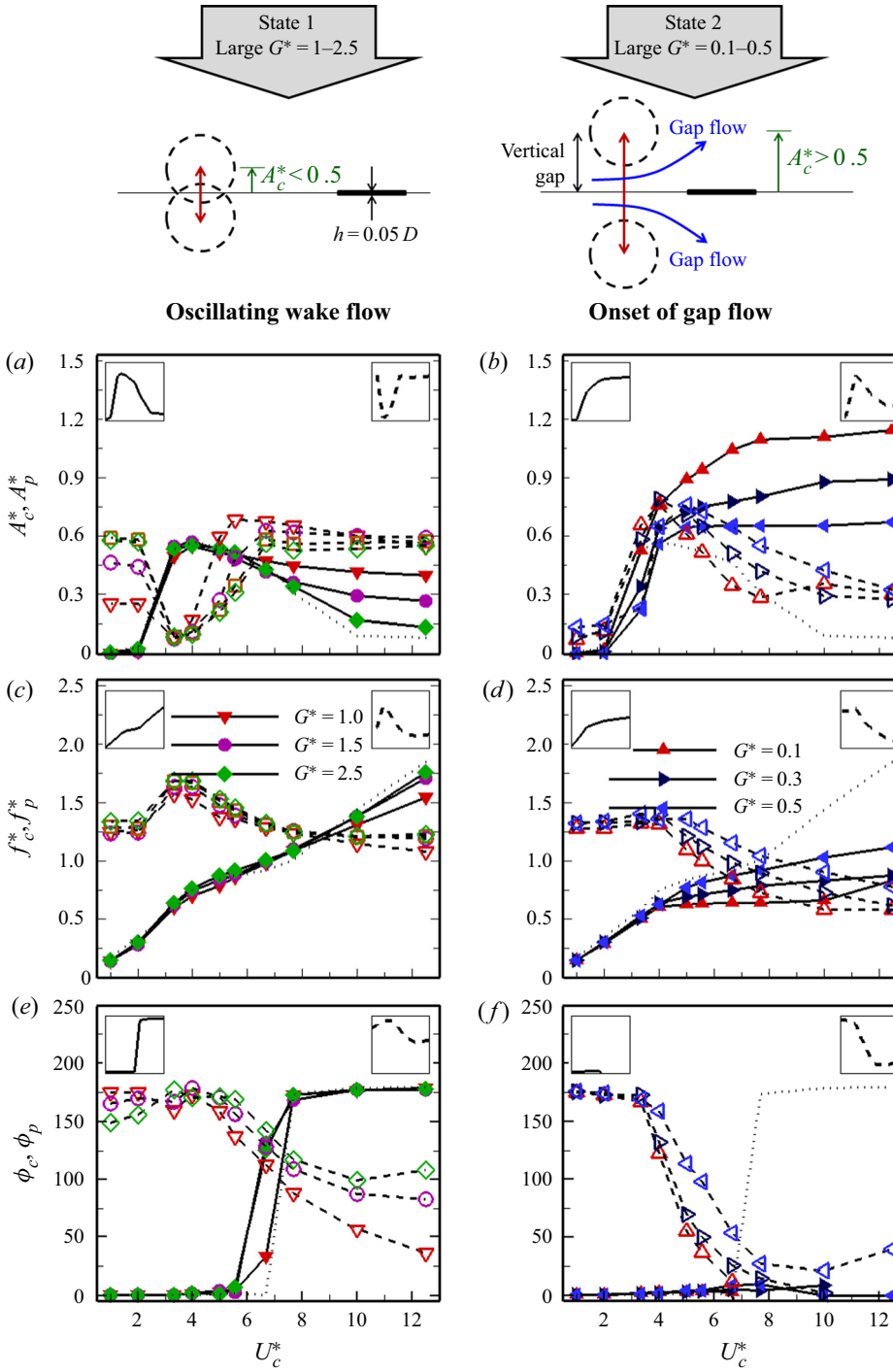

Figure 7. Variation of the cylinder and the plate vibrational (*a*,*b*) amplitude (A_c^* and A_p^*), (*c*,*d*) frequency ratio (f_c^* and f_p^*), and (*e*,*f*) phase difference (ϕ_c and ϕ_p), with increasing U_c^*, at (*a*,*c*,*e*) larger and (*b*,*d*,*f*) smaller gaps G^*. The vibration response is represented by solid lines for the cylinder and dashed lines for the plate, and the dotted lines show the response of an isolated elastically mounted cylinder. The legend in (*c*) applies to (*a*,*c*,*e*), and the legend in (*d*) applies to (*b*,*d*,*f*). The schematics at the top of the figure show the proximity-induced two states of the FICV characteristics.

The effect of the proximity-based transition in the flow regime is also reflected in the frequency response of the system, expressed in terms of frequency ratios: $f_c^* = f_c/f_{n,c}$ for the cylinder, and $f_p^* = f_p/f_{n,p}$ for the plate. Note that the natural frequency $f_{n,c} = 1/U_c^*$ of vibration of the cylinder varies with U_c^*. However, for first-mode vibrations of a cantilever-beam-like flexible plate of constant structural and geometrical properties considered here, $f_{n,p} = 0.5595\sqrt{K_b/L^*t^*\rho^*} = 0.1147$ is constant for the plate. For the present FMSI system, the cylinder oscillation frequency f_c always locks in with the oscillation frequency f_p of the plate at the periodic state. Hence the variation of f_p^* represents the variation of actual frequency of the cylinder–plate system since $f_{n,p}$ is constant. For state 1, figure 7(*c*) shows that the frequency ratio f_c^* of the cylinder shows a variation similar to that of an isolated cylinder (figure 4*b*). However, a slight variation in both f_c^* and f_p^* can be seen in state 1. As the plate is brought closer to the cylinder, the onset of the gap flow probably leads to a transition in the frequency response f_c^* of the cylinder (figure 7*d*), from an increasing VIV trend of variation in state 1 to a plateau variation in state 2. The oscillation frequency of the cylinder–plate system, represented by f_p^*, decreases with decreasing gaps G^* as seen in figures 7(*c*,*d*). This behaviour is in contrast to the cylinder amplitude A_c^*, which increases with decreasing gaps (figure 7*b*). The onset of gap flow observed in state 2 correlates with the galloping phenomenon (discussed in § 5.2), which is associated with lower oscillation frequency ($f_c = f_p$) of the cylinder–plate system. Low-frequency vibrations in the case of galloping are well reported in the literature (Bokaian & Geoola 1984*a*; Sahu *et al.* 2019). The nearly constant f_c^* observed in the case of the galloping response in state 2 resembles that observed for the galloping region in the past studies on VIV of tandem cylinders (Bokaian & Geoola 1984*a*) and on VIV of a cylinder with an attached flexible plate (Sahu *et al.* 2019).

Similar to the amplitude and the frequency response, the phase difference ϕ_c (between the temporal variation of transverse displacement $Y_c(\tau)$ and lift coefficient $C_{L,c}(\tau)$) variation in state 1 (figure 7*e*) resembles that of an isolated cylinder. In this state, figure 7(*e*) shows a sharp transition from in-phase ($\phi_c \approx 0^\circ$) to anti-phase variation ($\phi_c \approx 180^\circ$) with increasing U_c^*. Such a phase jump for ϕ_c is not observed in figure 7(*f*) at the smaller G^*. The absence of the jump-associated damping may be a reason for almost no decay of A_c^*, and the corresponding galloping response at the larger U_c^* in state 2, as discussed below. At smaller U_c^*, figures 7(*e*,*f*) show a nearly anti-phase $\phi_p \approx 180^\circ$ variation for the plate, in contrast to the nearly in-phase $\phi_c \approx 0^\circ$ variation for the cylinder. Further, with increasing U_c^*, figure 7(*f*) shows a transition from anti-phase $\phi_p \approx 180^\circ$ to in-phase $\phi_p \approx 0^\circ$ variation for the plate. With increasing U_c^*, note from figures 7(*e*,*f*) that the trend of variation of ϕ_p is similar at both larger and smaller G^*, in contrast to the dissimilar trend for the variation of ϕ_c. Also, at larger G^*, figure 7(*e*) shows an opposite transition of the phase for the cylinder, as compared to that for the plate.

For a larger gap $G^* = 2.5$ and $U_c^* = 12.5$, figure 7(*e*) shows $\phi_p \approx 110^\circ$ for the phase difference between the temporal variation of space-averaged lift coefficient $C_{L,p}$ and displacement Y_p of the tip of the plate, with first-mode vibrations for all the cases considered here. Here, the phase difference between the local lift coefficient C_L^{local} and local plate displacement Y_p^{local} (no figure shown here) is found to be almost in-phase near the leading edge and anti-phase near the trailing edge of the plate. Further, for a smaller gap $G^* = 0.3$ and $U_c^* = 7.7$, figure 7(*f*) shows $\phi_p \approx 14^\circ$, where an almost in-phase variation of C_L^{local} and Y_p^{local} is found for various points on the plate.

5. Flow-regimes-based flow-induced damping mechanisms for the transition in the FICV characteristics of the cylinder

The FICV characteristics of the cylinder show distinct amplitude responses in states 1 and 2, with VIV-type and galloping-type responses in the respective states (figures 4*a*,*b*). As discussed above, this transition in the structural dynamics is caused by the transition in the fluid dynamics behind the cylinder – oscillating wake flow in state 1 to the onset of gap flow in state 2. In the present section, the two types of flow regimes and the associated damping mechanisms, which lead to the transition in the cylinder structural dynamics and the onset of galloping, are presented. The flow-induced damping mechanisms are presented below in separate subsections for both flow regimes, with the help of temporal variation of velocity vectors and vorticity as well as velocity contours.

5.1. *Oscillating wake flow in state 1*

For a representative case of $G^* = 2.5$ and $U_c^* = 12.5$ in state 1, figures 8(c_1–c_5) show a vertically oscillating wake flow behind the cylinder, where the non-dimensional streamwise velocity upstream of the plate is less than 1 at all time instants. Due to the larger gap between the two structures in state 1, figures 8(a_1–a_5) and 8(b_1–b_5) show that the cylinder vortices are formed completely within the gap before they interact with the plate. Figure 8(*e*) shows an anti-phase variation in the cylinder displacement $Y_c(\tau)$ and lift coefficient $C_{L,c}(\tau)$.

For the cylinder at the topmost position, figures 8(a_1,b_1) show the formation of a counter-clockwise (CCW) vortex on the rear surface of the cylinder. This CCW vortex in the bottom half leads to a downward force, as seen by the negative value of $C_{L,c}$ in figure 8(*d*). Furthermore, figures 8(a_1–a_5) correspond to a downward motion of the cylinder, and an anti-phase upward motion is seen for the plate. The upward-moving plate sweeps the surrounding fluid during the downward movement of the cylinder. The void created below the plate causes a larger entrainment of the fluid, which results in a stronger CCW vortex. The sweeping and the entrainment of the surrounding fluid as well as the resulting larger CCW vortex are marked in figures 8(b_2,b_3). This flow phenomenon indicates that the cylinder acquires a larger momentum along its motion from the topmost to the mean position (figures 8a_1–a_3). However, as the cylinder drives past the mean position, figure 8(*d*) shows a change in the direction of $C_{L,c}$ from downwards to upwards due to the newly formed clockwise (CW) vortex on the rear surface of the cylinder. As shown by the marked arrows on the cylinder for the $C_{L,c}$ in figures 8(b_1–b_5), the flow-induced lift force always tries to bring the cylinder inwards (towards the mean position) at any point in its oscillation. Thus the lift force is a restoring force that always opposes the outward motion of the cylinder, i.e. the cylinder is subjected to flow-induced positive damping.

The positive damping on the cylinder in state 1, due to the anti-phase variation of Y_c and $C_{L,c}$, is similar to that reported earlier for FIV of an isolated cylinder (Williamson & Govardhan 2004; Prasanth & Mittal 2008). The flow-induced damping and the small value of $C_{L,c}$ at large U_c^* act as an amplitude-limiting mechanism (Blackburn & Karniadakis 1993) and result in the reduction in amplitude A_c^* at the larger U_c^*. However, the favourable sweeping action of the plate aids the formation of stronger vortices behind the cylinder, as compared to an isolated cylinder, which results in a relatively larger lift force and a proximity-induced increase in the cylinder amplitude at larger U_c^* (figure 7*a*). This favourable upward (downward) sweeping of fluid away during the downward (upward)

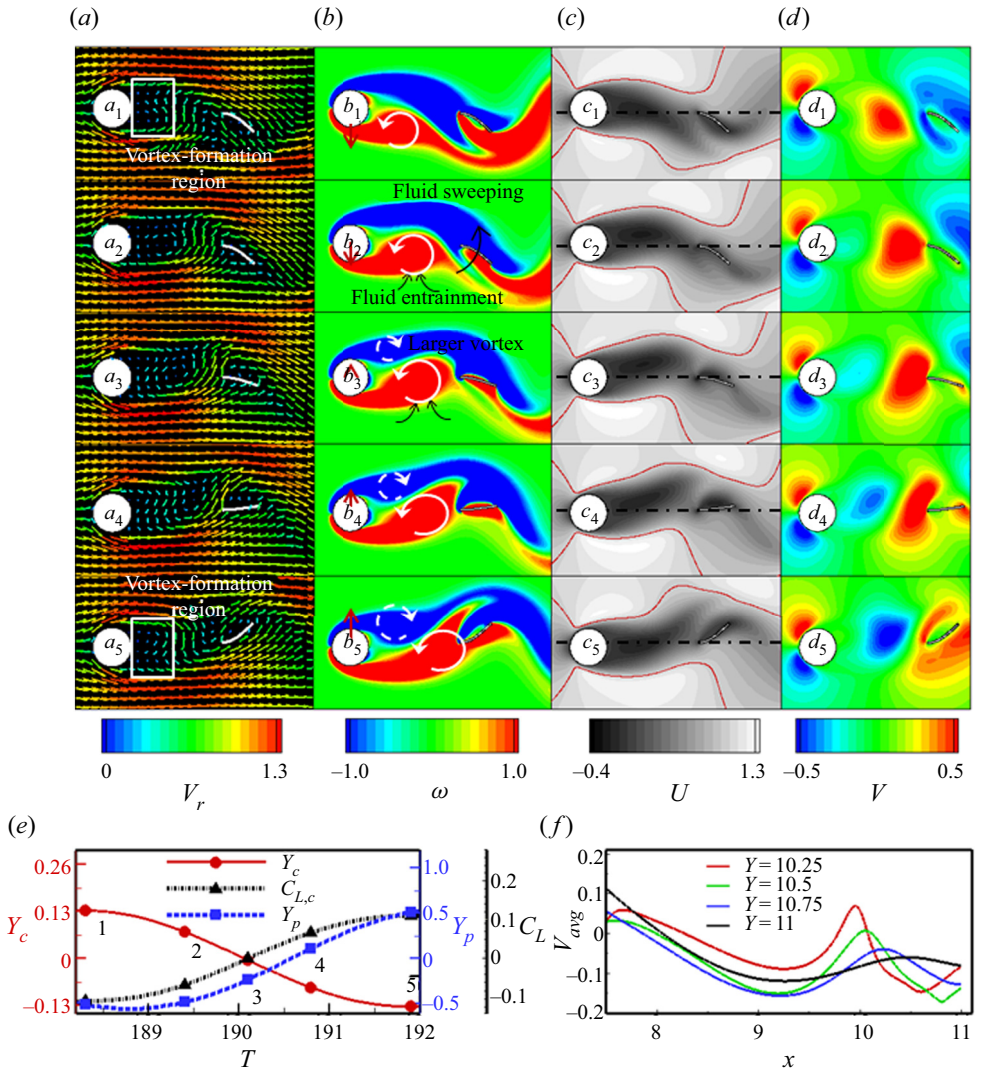

Figure 8. Timewise variation of (*a–d*) flow structures; (*e*) structural displacement (Y_c and Y_p) as well as lift coefficient $C_{L,c}$ of the cylinder; and (*f*) time-averaged V velocity profiles at various transverse Y locations above the plate, within a half-cycle of periodic motion, corresponding to the cylinder motion from the topmost to the bottommost position, at $U_c^* = 12.5$ and $G^* = 2.5$ in state 1. Sub-panels (a_1–a_5), (b_1–b_5), (c_1–c_5) and (d_1–d_5) show the velocity vectors coloured with the magnitude of resultant velocity, vorticity contours, streamwise U velocity contours, and V velocity contours, respectively. The vertical arrow in (b_1–b_5) represents the relative magnitude and direction of $C_{L,c}$, and the line in (c_1–c_5) represents a line contour with $U = 1$. The flow structures correspond to the time instants marked 1–5 in (*e*).

motion of the cylinder is brought about by an out-of-phase ($\phi_{c,p} \geqslant 90°$) motion of the plate with respect to the cylinder motion. Further, a cylinder-oscillation-induced upward and downward flow, near the leading edge of the plate, is shown by instantaneous V velocity contours in figure 8(*d*) and time-averaged V velocity profiles in figure 8(*f*).

5.2. *Onset of gap flow in state 2*

For a representative case of $G^* = 0.3$ and $U_c^* = 7.7$ in state 2, figures 9(a_1–a_5) and 9(d_1–d_5) show the formation of a cylinder-oscillation-induced upward/downward flow closer to the cylinder, due to the creation of a vertical gap between the two structures when the instantaneous cylinder amplitude is $A_c^* > 0.5$. The vertically oscillating flow is shown more clearly by the time-averaged V velocity profile in figure 9(f). With increasing Y location, the figure shows that the peak of the V velocity profile decreases and shifts downstream along with an increase in the width of the high-velocity region. Although the vertically oscillating flow is also seen at larger G^* in figure 8(f), the maximum V velocity is relatively far away from the cylinder, and its value is smaller compared to that seen in figure 9(f) for smaller G^*. Thus the vertically oscillating flow is close to the cylinder and much stronger in state 2 as compared to state 1. The closer and stronger vertically oscillating flow is associated with an increase in the magnitude of lift force along with a transition from restoring to exciting force, as discussed below. Unlike state 1, figures 9(b_1–b_5) show that the cylinder vortices are not formed completely in state 2. Thus it can be seen that the plate interacts with a partially formed cylinder vortex, leading to a smaller oscillation amplitude of the plate A_p^*, which decreases with decreasing G^* ($\leqslant 0.5$).

At the topmost position of the cylinder, figures 9(a_1, b_1) show that a CCW vortex starts forming on the rear surface of the cylinder. The forming CCW cylinder vortex pairs with the CW vortex at the leading edge of the plate. This cylinder–plate CCW–CW vortices pairing results in a vertical gap-flow-based upward entrainment of the free-stream flow in the wake behind the cylinder. As the cylinder moves from the topmost to the mean position, figures 9(a_1–a_3) show that the gap-flow-based entrainment of the free-stream flow reduces, along with a reduction in the upward lift force (refer to the vertical arrow in figures 9b_1–b_3). However, when the cylinder crosses the mean position, the direction of the gap-flow-based entrainment switches from upwards to downwards (figures 9a_2–a_4), and the cylinder–plate vortex pairing transits from CCW–CW to CW–CCW (figures 9b_2–b_4), which leads to a change in the direction of the lift force from upwards to downwards (figures 9b_2–b_4 and 9d).

From the upward and downward lift forces discussed above, during the downward motion of the cylinder, note from the marked arrows on the cylinder that the instantaneous $C_{L,c}$ always tries to take the cylinder outwards (away from the mean position) at any point of its oscillation. Thus, in contrast to the above discussed restoring force at larger G^*, the lift force at smaller G^* is an excitation force that always aids the outward motion of the cylinder. This leads to a flow-induced negative damping, caused by the in-phase variation of Y_c and $C_{L,c}$ that results in the large-amplitude galloping phenomenon in state 2. This in-phase variation is a consequence of the pairing of the cylinder–plate vortices and the cylinder-oscillation-induced upward/downward flow close to the cylinder. The vertically oscillating flow is stronger when the plate moves almost in-phase with the cylinder, resulting in a very-high-amplitude galloping response of the cylinder.

Also note that the proximity interference leads to an upward (downward) roll-up of the CCW (CW) vortices on the rear surface of the cylinder, as seen in figures 9(b_1,b_2) (figures 9b_4,b_5) in state 2; this is not seen for the larger gaps in state 1 (figures 8b_1–b_5).

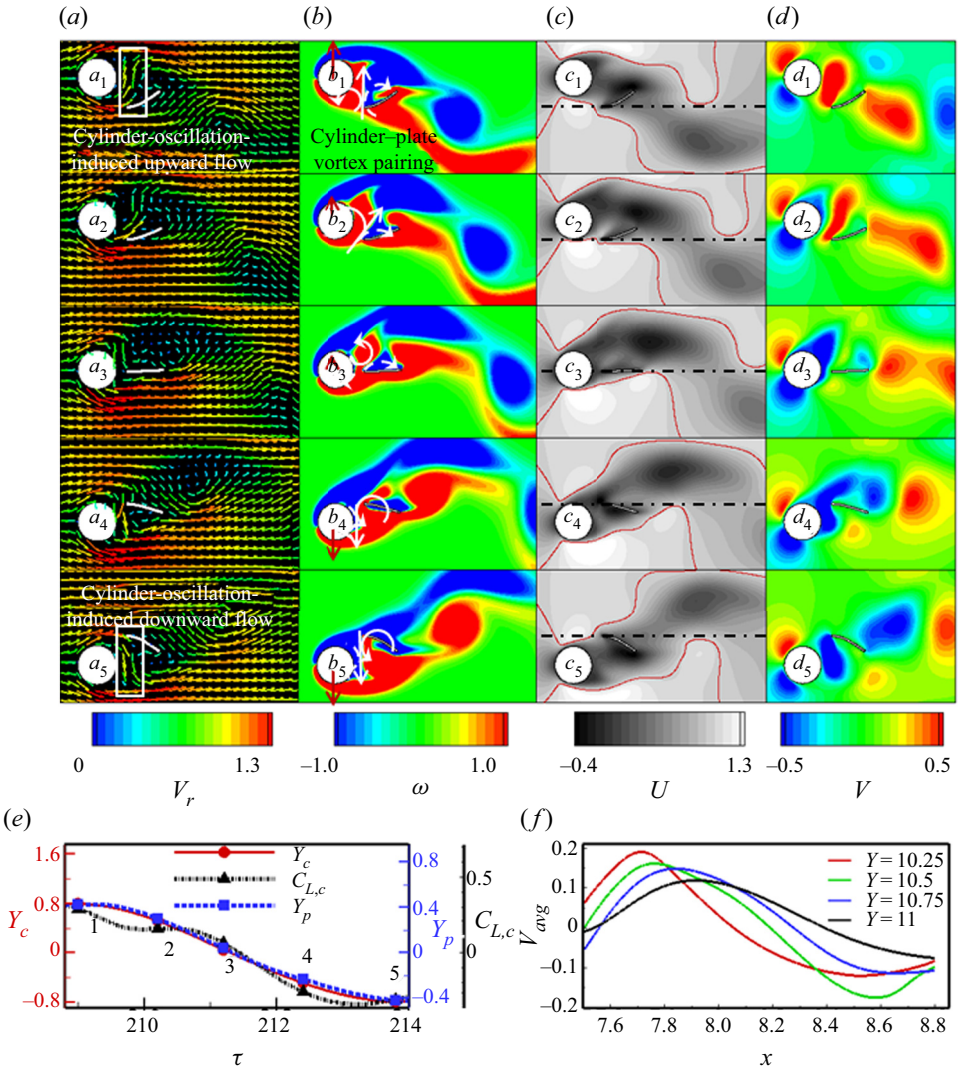

Figure 9. Timewise variation of (*a–d*) flow structures; (*e*) structural displacement (Y_c and Y_p) as well as lift coefficient $C_{L,c}$ of the cylinder; and (*f*) time-averaged V velocity profiles at various transverse Y locations above the plate, within a half-cycle of periodic motion, corresponding to the cylinder motion from the topmost to the bottommost position, at $U_c^* = 7.7$ and $G^* = 0.3$ in state 2. Sub-panels (a_1–a_5), (b_1–b_5), (c_1–c_5) and (d_1–d_5) show the velocity vectors coloured with the magnitude of resultant velocity, vorticity contours, streamwise U velocity contours, and V velocity contours, respectively. The vertical arrow in (b_1–b_5) represents the relative magnitude and direction of $C_{L,c}$, and the line in (c_1–c_5) represents a line contour with $U = 1$. The flow structures correspond to the time instants marked 1–5 in (*e*).

6. Effect of proximity interference on cylinder–plate vortex-interaction dynamics in the near wake

The previous section discussed the two flow regimes and the correlation of the associated flow structures with the cylinder amplitude response. This section presents the effect of the proximity interference on the interaction of the cylinder–plate vortices in the near wake; the resulting vortex-shedding patterns in the far wake are presented in the next section. The near wake results are presented below in separate subsections for smaller U_c^* and

larger U_c^*. Since the cylinder is almost stationary at smaller U_c^* (figure 5*a*), § 6.1 presents the effect of the near wake vortex-interaction dynamics on the mean recirculation length and plate vibrations. For the oscillating cylinder at intermediate and larger U_c^*, the cylinder–plate vortex-interaction dynamics is presented in § 6.2 with the help of a periodic variation of vorticity contours, cylinder displacement and plate displacement.

6.1. *Effect of vortex interference on mean recirculation length behind an almost stationary cylinder*

Due to very small amplitude of vibration of the cylinder at $U_c^* \leqslant 2$ (figure 5*a*), the results at smaller U_c^* can be discussed for FIV of a flexible plate in the wake of an almost stationary cylinder. In this subsection, the proximity interference effect on the plate vibrations and mean recirculation region behind the cylinder is presented for various gaps G^*.This mutual interaction between the plate and the surrounding flow in the wake region is discussed in this subsection.

A larger proximity interference is observed when the flexible plate is located very close to the cylinder and inhibits the interaction of the free shear layers above and below the cylinder. This results in a very large mean recirculation length L_r, as compared to the $L_{r,st}$ for an isolated stationary cylinder; more than double for $G^* = 0.1$, as shown in figure 10(*a*). Thus the plate lies well within the recirculation region, where it is subjected to a very low transverse velocity, and the plate oscillates with an extremely low amplitude. Figure 10(*b*) shows that L_r decreases with increasing gaps up to $G^* = 0.5$), which results in a gradually increasing A_p^* with increasing $G^* \leqslant 0.5$. Further increase in G^*, up to 1.5, causes insignificant change in L_r. However, with increasing gap G^*, the plate moves continuously out of the recirculation region, as shown in figure 10(*a*) for $G^* = 1.5$. Since the plate tip is outside the recirculation region, in a high transverse velocity region, a significant increase in A_p is observed in figure 10(*b*) for $G^* = 1.5$. At the gaps $G^* \leqslant 1.5$, the cylinder vortices are well attached to the plate. However, as the gap increases further to $G^* = 2$, the figure shows that the mean recirculation region shrinks drastically to $L_r < L_{r,st}$, as the cylinder vortices are no longer attached to the plate. This results in an increase in the plate amplitude, as seen in figure 10(*b*) at $G^* = 2$. Any further increase in G^* is seen to cause insignificant change in L_r as well as A_p^*.

The above results show that for the smaller gaps $G^* \leqslant 1.5$, the proximity interference increases the mean recirculation region as compared to that for an isolated cylinder. There exists a critical gap $G_c^* = 1.5$ beyond which the recirculation region shrinks drastically. This critical gap is much smaller than the critical gap $G_c^* = 2.6$ with a rigid plate in a similar configuration (Hwang *et al.* 2003), indicating that the structural flexibility of the plate aids the cylinder–plate vortex interaction and leads to the shrinkage of the mean recirculation region at a lower G^*.

6.2. *Cylinder–plate vortex-interaction dynamics for a vibrating cylinder*

At intermediate and high reduced velocity ($U_c^* > 2$), the cylinder oscillates with a substantial amplitude in both the states of FICV response (figures 7*a*,*b*). Thus the plate amplitude at these reduced velocities is governed primarily by the nature of interaction of the cylinder vortex with the plate vortex. In the present study, three types of cylinder–plate vortex interactions are observed: constructive, destructive and partial interaction. These vortex-interaction modes are discussed here, correlating the

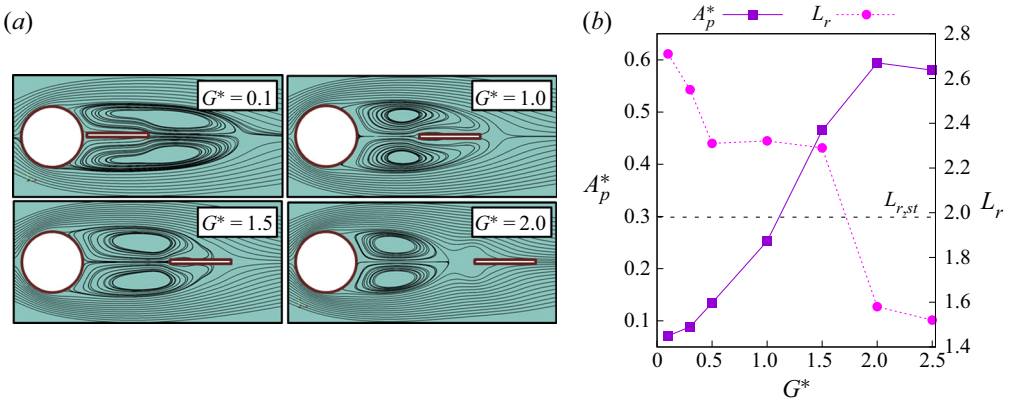

Figure 10. (*a*) Time-averaged streamlines and (*b*) variation of plate amplitude A_p^* and recirculation length L_r, with increasing cylinder–plate gaps G^*, for $U_c^* = 1$, where L_r is measured from the rear surface of the cylinder. The recirculation length $L_{r,st}$ for an isolated stationary cylinder is represented by a dashed line in (*b*).

effect of the vortex interactions on the plate amplitude. The vortex interactions are studied with the help of a timewise variation of vorticity contours and cylinder/plate displacement (Y_c/Y_p) over a half-cycle of the periodic motion, as shown in figure 11.

The destructive interaction is shown in figure 11(*a*) for a representative case that corresponds to $U_c^* = 5.5$ and $G^* = 2.5$. When the cylinder is at the mean position, figure 11(a_1) shows that a CCW cylinder vortex 'I' reaches the tip of the flexible plate and interacts with a CW plate vortex 'i'. Figures 11(a_1–a_4) show that the opposite-signed cylinder–plate vortex interaction leads to a weakening and finally the dissipation of the plate vortex 'i'. Simultaneously, the figure shows that a CW cylinder vortex 'II' advects along the upper surface of the plate and interacts with a CCW plate vortex 'ii'. Since the vortex interaction involves opposite-signed cylinder and plate vortices, this type of two-structure vortex interaction is called the destructive interaction (Gopalkrishnan *et al.* 1994). It results in a small lift force on the plate and consequently a smaller plate amplitude (figure 6*a*). The plate-tip vortex, formed during the destructive interaction, is very weak and gets dissipated without causing any significant change in the vortex-shedding pattern, presented in the next subsection.

The constructive interaction is shown in figure 11(*b*) for a representative case at $U_c^* = 6.7$ and $G^* = 2.5$. At the mid-position of the cylinder, figure 11(b_1) shows a CW cylinder vortex 'I' at the leading edge of the plate, which interacts with a CW plate vortex. Later, figures 11(b_3,b_4) show that the two same-signed CW vortices coalesce together forming a CW vortex 'Ii'. Simultaneously, as the coalesced cylinder–plate vortex 'Ii' advects, the figure shows the growth of a CCW plate vortex 'ii' at the trailing edge of the plate that would interact with the incoming cylinder vortex 'II'. Since the interaction involves same-signed vortices, this type of two-structure vortex interaction is called the constructive interaction (Gopalkrishnan *et al.* 1994). It leads to a large lift force on the plate and results in a larger plate amplitude (figure 6*a*). Since the cylinder and plate vortices coalesce during a constructive interaction, this type of interaction (similar to the destructive interaction) does not affect the vorticity pattern in the wake region, presented in the next subsection.

The partial interaction is shown in figure 11(*c*) for a representative case at $U_c^* = 12.5$ and $G^* = 1$. When the cylinder is at the mean position, figure 11(c_1) shows the formation

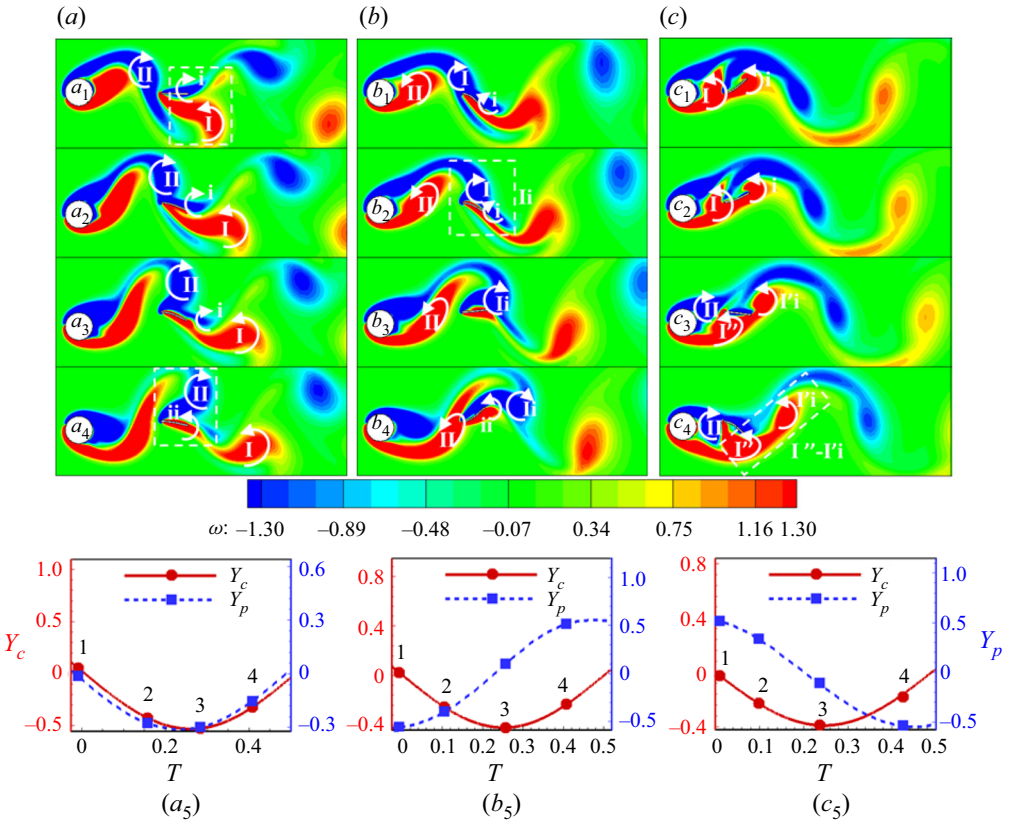

Figure 11. Vorticity contours over a half-cycle of periodic motion of the two structures, corresponding to the cylinder motion from the mean position to the bottommost and finally back to the mean position, at (a_1–a_4) $U_c^* = 5.5$ and $G^* = 2.5$, (b_1–b_4) $U_c^* = 6.7$ and $G^* = 2.5$, and (c_1–c_4) $U_c^* = 12.5$ and $G^* = 1.0$. The contours correspond to the time instants marked 1–4 in (a_5), (b_5) and (c_5), which show the temporal variation of cylinder displacement Y_c and plate displacement Y_p.

of a CCW cylinder vortex 'I' and a CCW plate vortex 'i'. As the vortex 'I' advects downstream, figure 11(c_3) shows that the plate vortex is fed by the same-signed vorticity of the cylinder vortex 'I'. Thus figures 11(c_1–c_3) show that the CCW plate vortex 'i' interacts and grows in size as 'I′i' with some part of the same-signed CCW cylinder vortex. Later, figure 11(c_4) shows that the remaining part of the CCW cylinder vortex 'I″' interacts with the opposite-signed CW plate vortex. The above cylinder–plate vortex interaction involves the constructive and destructive interactions in sequence, and is called here the partial interaction. The partial cylinder–plate vortex interaction results in the formation of a CCW vortex pair, marked as 'I″-I′i' in figure 11(c_4). Later, as the initiation of shedding of the CCW vortex commences downstream of the cylinder, the vortex pair 'I″-I′i' breaks and sheds the vortices 'I″' and 'I′i' as two distinct CCW vortices for certain cases, while for the other cases, the coalesced vortex pair is shed. The respective cases result in a vortex-shedding pattern called here 2P (two pairs of shed vortices) and C(2P) (coalesced two-pairs) modes of vortex shedding. The larger the distance between the vortex pair, the weaker the vortex interaction and consequently the smaller the plate amplitude.

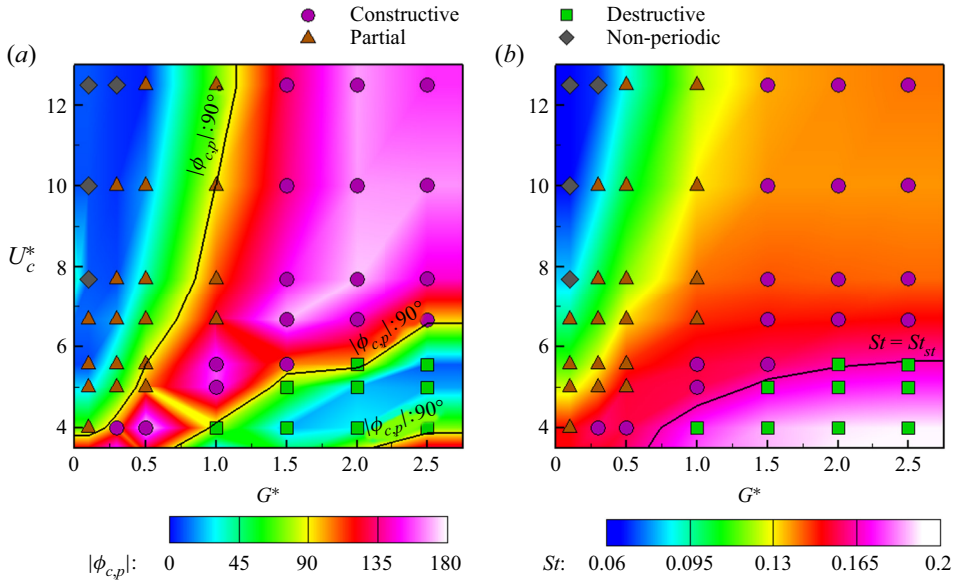

Figure 12. Cylinder–plate vortex-interaction regime map. Contours of (*a*) absolute value of phase difference $|\phi_{c,p}|$ between cylinder displacement Y_c and plate displacement Y_p, and (*b*) non-dimensional vortex-shedding or oscillation frequency (Strouhal number St). Here, St_{st} is the non-dimensional vortex-shedding frequency of a stationary cylinder.

The constructive and destructive vortex interactions discussed above were proposed by Gopalkrishnan *et al.* (1994) for an FMSI problem on flow across a rigid aerofoil with a prescribed pitching and heaving motion, and a downstream heaving cylinder. As compared to the forced motion of the rigid structures in their work, the present work is based on flow-induced vibration of the two structures (one rigid and the other flexible), and the correlation between the vortex interactions and the plate amplitude is presented here probably for the first time. Constructive and destructive interactions were also reported for forced oscillation of a flexible plate behind a cylinder (Wu *et al.* 2014); however, the partial interaction is not found in the literature and is proposed in the present work.

6.3. *Cylinder–plate vortex-interaction dynamics based regime map*

Figure 12 shows the regime map for the vortex-interaction modes discussed above. The map shows a demarcation of the vortex-interaction modes, with each mode corresponding to the contour value of certain quantitative parameters – phase difference $\phi_{c,p}$ (between the FICV of the two structures) and the non-dimensional vortex-shedding frequency St. The figure shows that the destructive interaction occurs at intermediate values of U^* ($\approx 4-6$) and larger gap ($G^* \geqslant 1.0$), while the partial and constructive interactions occur at intermediate as well as larger U_c^*. Partial interaction is observed only at smaller gaps ($G^* \leqslant 1.0$), and constructive interaction is observed for almost all the gaps ($G^* \geqslant 0.3$). With increasing U_c^*, note that the vortex-interaction mode transits from destructive to constructive at larger G^*, and it transits from constructive to partial at smaller G^*.

Figure 12(*a*) shows that each vortex-interaction mode is correlated closely with the phase difference between the transient vibrations of the two structures. The figure shows

that the cylinder and plate vortices undergo constructive interaction when the two structures oscillate with $|\phi_{c,p}| = 90^\circ$ to 180°. However, for $|\phi_{c,p}| = 0^\circ$ to 90°, the vortices undergo destructive interaction at larger gaps ($G^* \geqslant 1.0$) and partial interaction at smaller gaps ($G^* \leqslant 1.0$). Although the figure shows the variation of absolute value of $\phi_{c,p}$, it is worth pointing out that the destructive interaction almost corresponds to $\phi_{c,p} \approx -90^\circ$ to 90°, the partial interaction corresponds to $\phi_{c,p} \approx 0^\circ$ to -90°, and the constructive interaction corresponds to $\phi_{c,p} \approx 90^\circ$ to 180° as well as $\phi_{c,p} \approx -90^\circ$ to -180°. For the transition from $\phi_{c,p} = 180^\circ$ to -180°, which corresponds to $|\phi_{c,p}| = 180^\circ$ in figure 12(*a*), note that the corresponding U_c^* for $G^* \geqslant 0.5$ in the figure almost matches with the U_c^* for the proximity-induced deviation of A_c^* in figure 5(*a*).

Note that the above demarcating values of $|\phi_{c,p}|$ are representative, and there are a few exceptions for the partial interaction with $|\phi_{c,p}| > 90^\circ$, corresponding to $G^* = 1.0$ ($U_c^* = 6.7$ and 7.7) and $G^* = 0.5$ ($U_c^* = 5.0$). However, these exceptions are close to the transition from state 1 ($G^* = 1$) to state 2 ($G^* = 0.5$) of FICV characteristics. Also note that the $\phi_{c,p} = 0^\circ$ to -90° values, for the partial interaction, overlap with those for the destructive interaction. However, the two regimes are demarcated by the values of vortex-shedding/oscillation frequency, i.e, $St < St_{st}$ for the partial interaction, and $St \geqslant St_{st}$ for the destructive interaction, as shown in figure 12(*b*). The figure shows that the destructive, constructive and partial vortex interactions are larger, intermediate and smaller frequency phenomena. Thus the increased cylinder–plate proximity interference leads to a decrease in the frequency of the two-structure system. The high cylinder amplitude region in the VIV characteristics (for state 1) corresponds to a high-frequency phenomenon with $St > St_{st}$, while the galloping amplitude response (in state 2) corresponds to a low-frequency phenomenon with $St < St_{st}$. The demarcation of the various regimes in the map corresponds to:

(i) destructive vortex interaction: $|\phi_{c,p}| = 0^\circ$ to 90° and $St \geqslant St_{st}$
(ii) constructive vortex interaction: $|\phi_{c,p}| = 90^\circ$ to 180° and $St < St_{st}$
(iii) partial vortex interaction: $|\phi_{c,p}| = 0^\circ$ to 90° and $St < St_{st}$.

It is worth noting that the regime map in figure 12 presents a quantitative identification of the cylinder–plate vortex-interaction mode as compared to the qualitative identification observed in figure 11. Such a quantitative identification of the vortex-interaction modes is not available in the literature.

7. Effect of the cylinder–plate vortex interaction on the vortex-shedding patterns in the far wake

The cylinder–plate vortex interference in the near wake affects significantly the vortex-shedding patterns behind the two structures in the far wake. The effect is predominant in state 2, where the proximity interference effects are dominant. In the present work, four types of vortex patterns are observed: 2S, C(2S), 2P and C(2P), as shown in figure 13. The 2S pattern refers to two single opposite-signed shed vortices per cycle of cylinder oscillation. Here, the wake consists of a staggered arrangement of opposite-signed vortices in a single row (figure 13*a*). The C(2S) pattern is a coalesced-2S pattern, where the same-signed vortices coalesce and a double row of vortices is observed (figure 13*b*). The 2P pattern refers to two pairs of opposite-signed vortices shed per cycle of the cylinder oscillation, with four distinct vortices in the wake for each cycle (figure 13*c*). The C(2P) pattern is a coalesced-2P pattern, where the same-signed vortices in each pair

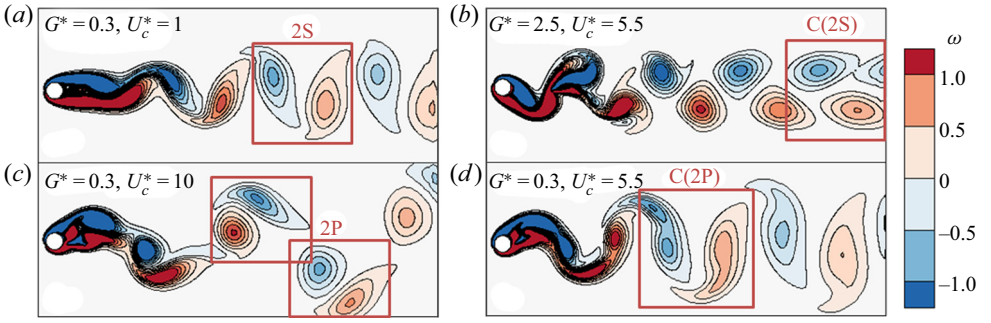

Figure 13. Instantaneous vorticity contours of the various vortex patterns observed in the present work: (*a*) two single, 2S; (*b*) coalesced-2S, C(2S); (*c*) two pairs, 2P; and (*d*) coalesced-2P, C(2P).

of vortices, generated by the cylinder and plate, coalesce. Figure 13(*d*) shows that as the coalesced vortex pairs advect downstream, the plate vortex forms the head of the CW (CCW) coalesced vortex, closely resembling a transversely elongated 2S vortex pattern. This is in contrast to the 2P pattern, where the coalesced vortex pairs in the near wake break as they advect downstream. Although both C(2S) and C(2P) patterns involve coalescence of same-signed vortices, note that the coalescence occurs in the streamwise direction for C(2S), while it occurs in the transverse direction for C(2P).

The vortex-shedding patterns 2S, C(2S) and 2P are presented, using the terminology introduced by Williamson & Roshko (1988) for the forced motion of a circular cylinder. However, the present two pairs of shed vortices in the 2P mode correspond to each pair shed by the cylinder and the plate as compared to the two pairs shed by the cylinder in the proposition by Williamson & Roshko (1988). Moreover, the C(2P) mode of vortex shedding is proposed here and presented for the first time in the literature.

7.1. *Vortex-shedding patterns in state 1*

For the oscillating wake flow at a larger gap G^* in state 1, the cylinder and plate are widely spaced, leading to weak interaction between the two structures. Thus the vortex patterns in this state are dominated primarily by the upstream cylinder and closely resemble those of the FIV of an isolated cylinder ($G^* = \infty$).

Figure 14 shows the vortex shedding, downstream of both structures, with a 2S vortex-shedding pattern at low U_c^* (= 1). With an increase in the reduced velocity to $U_c^* = 3.3$, the cylinder amplitude A_c^* increases (figure 7*a*) and results in an increase in the transverse spacing between the vortices, which leads to a change in vortex pattern from 2S to C(2S). The C(2S) mode of shedding is sustained with further increase in U_c^*, up to 5.5, that corresponds to a larger cylinder amplitude (figure 7*a*). For $U_c^* > 5.5$, figure 7(*a*) shows a sharp decrease in A_c^* that leads to a transition from C(2S) to 2S mode for $G^* > 1$ (figure 14). The smaller A_c^* (at $U_c^* > 5.5$) does not lead to the two rows of shed vortices and coalescence. Thus in state 1, the figure shows that the wake gradually transitions from the C(2S) mode (for the high cylinder amplitude at the intermediate U_c^*) to the 2S mode of vortex shedding (for the low cylinder amplitude at smaller and larger U_c^*). We found that the downstream distance at which coalescence occurs in the C(2S) regime increases with increasing U_c^* and decreasing G^*. The coalescence is not observed for certain cases of the C(2S) regime in the figure (corresponding to larger U_c^* and smaller G^*) due to the shorter downstream distance considered in figure 14.

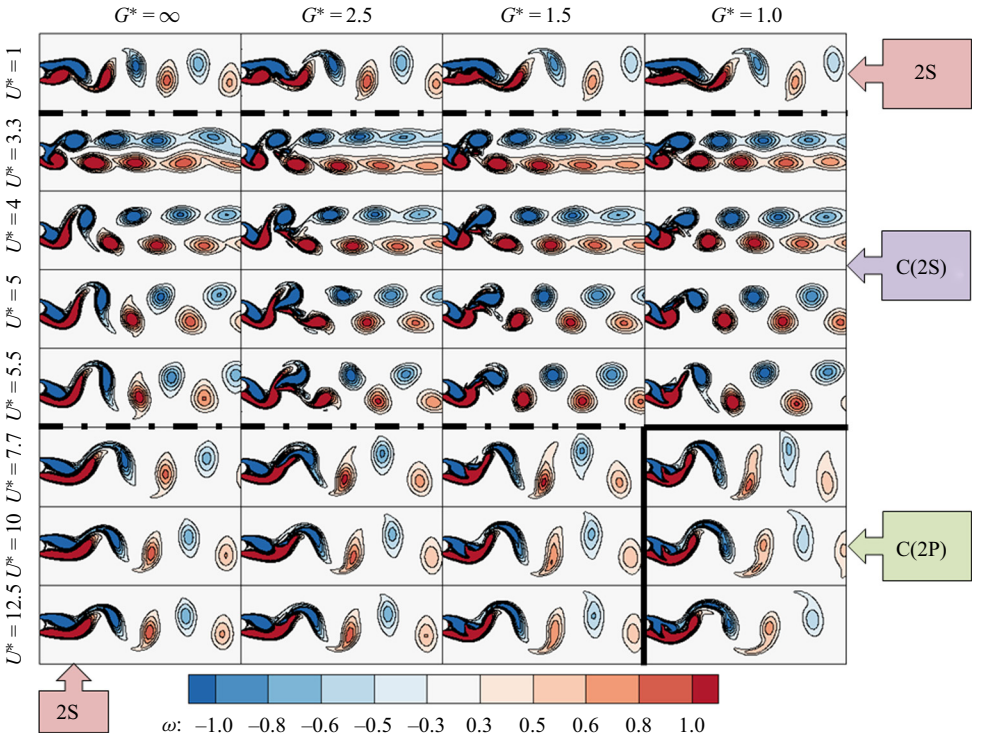

Figure 14. Instantaneous vorticity contours at various cylinder–plate gaps G^* and reduced velocity U_c^* for state 1. The vortex-shedding patterns are presented for the instant when the cylinder is at its mean position. The dash-dot lines demarcate the 2S and C(2S) patterns, and the solid line demarcates the C(2S) and C(2P) patterns.

The transition of the vortex-shedding pattern from 2S to C(2S) and gradually back to 2S, with increasing U_c^*, is well reported in past studies on FIV of an isolated cylinder at low *Re* (Leontini *et al.* 2006; Prasanth & Mittal 2008). However, as the cylinder–plate gap decreases to $G^* = 1.0$, the proximity-effect-based cylinder–plate vortex interaction starts dominating, with a larger plate amplitude at larger U_c^* (figure 7*a*), and the figure shows a transition from C(2S) to C(2P) modes of vortex-shedding pattern at the larger U_c^*. The C(2P) mode of vortex shedding is formed due to the partial interaction of the cylinder and the plate vortices, presented in figures 11(c_1–c_5).

7.2. *Vortex-shedding patterns in state 2*

Due to the onset of gap flow in state 2, the coupling between the displacement of the cylinder and the plate intensifies and leads to different vortex-shedding patterns as compared to the FIV of an isolated cylinder. At smaller reduced velocity U_c^*, figure 15 shows that the vortices arrange in the 2S pattern, similar to that for an isolated cylinder. The figure shows that the 2S pattern persists over a larger range of U_c^* in state 2, as compared to that in state 1 (figure 14). Contrary to the vortex-shedding patterns in state 1, figure 15 shows that the 2S pattern in state 2 transits almost directly from the 2S to the C(2P) pattern with increasing U_c^*. At larger U_c^*, the figure shows that the plate splits the coalesced

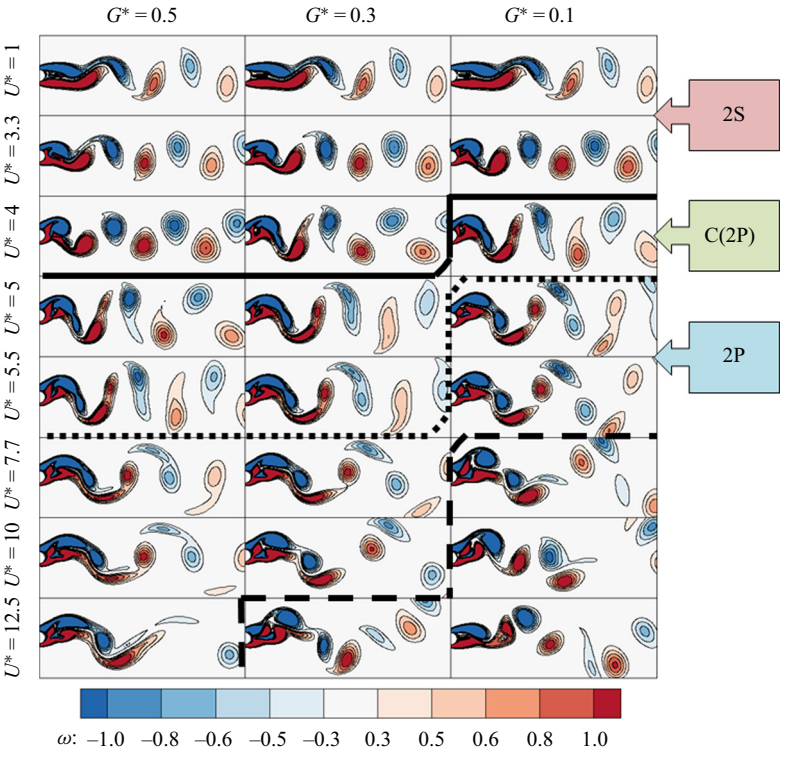

Figure 15. Instantaneous vorticity contours at different cylinder–plate gaps and reduced velocities for state 2. The vortex-shedding patterns are presented for the instant when the cylinder is at its mean position. The solid line demarcates the 2S and C(2P) patterns, the dotted line demarcates the C(2P) and 2P patterns, and the dashed line demarcates the 2P and non-periodic vortex-shedding patterns.

cylinder–plate C(2P) vortices (in the near wake) into 2P vortices (in the far wake), at a certain downstream distance. However, the downstream distance for the splitting is found to depend on the values of U_c^* and G^*. Although the transition from C(2P) to 2P mode (as the vortices move downstream) is not seen in figure 15 (for certain cases) due to a smaller downstream distance in the figure, the vortex splitting at a larger downstream distance is ensured for these cases (not shown here). At very low cylinder–plate gaps G^* and high U_c^*, the wake finally turns non-periodic with no discernible pattern, as shown in figure 15.

The 2P pattern obtained in the present work (at low *Re*) resembles that reported for the FIV of an isolated cylinder (at high *Re*) (Williamson & Govardhan 2004). However, it must be noted that the mechanism of formation of the 2P mode in the present low *Re* case is different from that reported for the isolated cylinder at high *Re*. The 2P vortex pattern was also reported by Borazjani & Sotiropoulos (2009) in their study on FIV of tandem cylinders at low *Re* (= 200). However, the 2P pattern for the FIV of the cylinder–plate system is shown here probably for the first time in the literature.

7.3. *Vortex-shedding pattern based regime map*

Figure 16 shows a vortex-shedding pattern based regime map, demarcating the various vortex-shedding regimes, overlapped with the contours of amplitude response of the

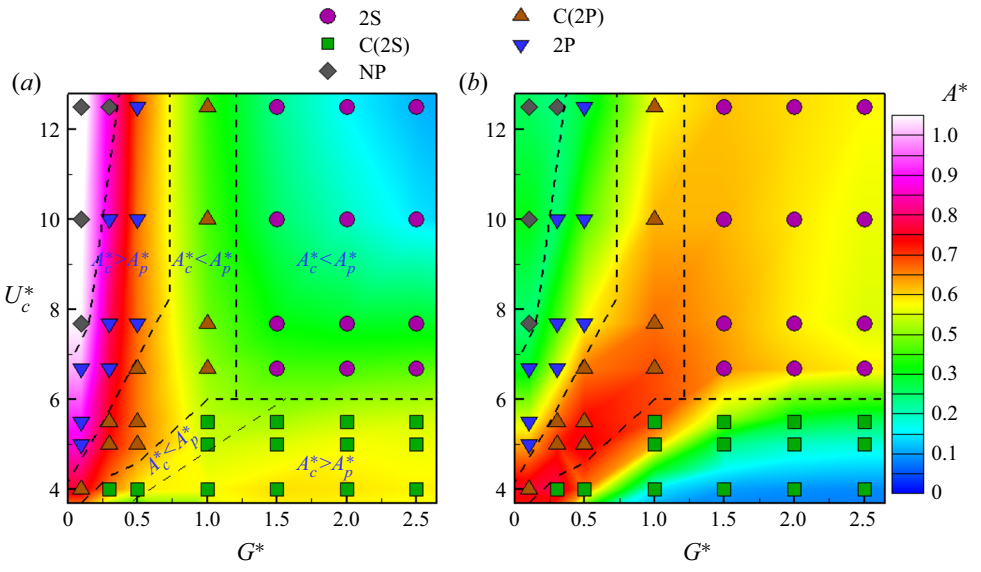

Figure 16. Vortex-shedding pattern based regime map, for various reduced velocities U_c^* and cylinder–plate gaps G^*, overlapped with the contours of vibrational amplitude of (*a*) the cylinder, A_c^*, and (*b*) the plate-tip, A_p^*.

two structures. The regime map is presented for $U_c^* \geqslant 4$ since the cylinder–plate proximity interference effect is seen at these U_c^* values; and A_c^* and A_p^* are large enough (figure 7) to have a significant effect on the vortex-shedding regime.

Figure 16 shows that the various vortex-shedding regimes are correlated strongly with the amplitude of the cylinder and the plate. In state 1, for larger gaps ($G^* \geqslant 1.0$), the cylinder oscillates with a large amplitude $A_c^* \geqslant A_p^*$ at the intermediate U_c^* that results in the formation of a C(2S) vortex-shedding pattern. At the larger U_c^* in state 1, the plate amplitude increases drastically with $A_p^* > A_c^*$, and results in the formation of a single row of vortices with a 2S pattern. With decreasing gap G^*, as the flow transitions from oscillating wake flow (state 1) to the onset of gap flow (state 2), the figure shows various transitions for state 2 at smaller gap – C(2S) to C(2P) and then to 2P, and finally non-periodic vortex-shedding regimes. The demarcation of the various vortex-shedding regimes in the map is as follows.

(i) 2S vortex shedding: larger G^* ($\geqslant 1.5$), larger U_c^* (> 6) and $A_p^* > A_c^*$.
(ii) C(2S) vortex shedding: intermediate U_c^* (< 6), and larger G^* (with $A_c^* > A_p^*$) as well as smaller G^* (with $A_c^* < A_p^*$).
(iii) C(2P) vortex shedding: smaller G^* ($\leqslant 1.0$) and $A_c^* < A_p^*$.
(iv) 2P vortex shedding: smaller G^* ($\leqslant 0.5$) and $A_c^* > A_p^*$.

8. Summary and conclusions

Figure 17 shows a graphical summary of the proximity-induced flow physics and the resulting vibration characteristics for the present FMSI system. The figure shows that

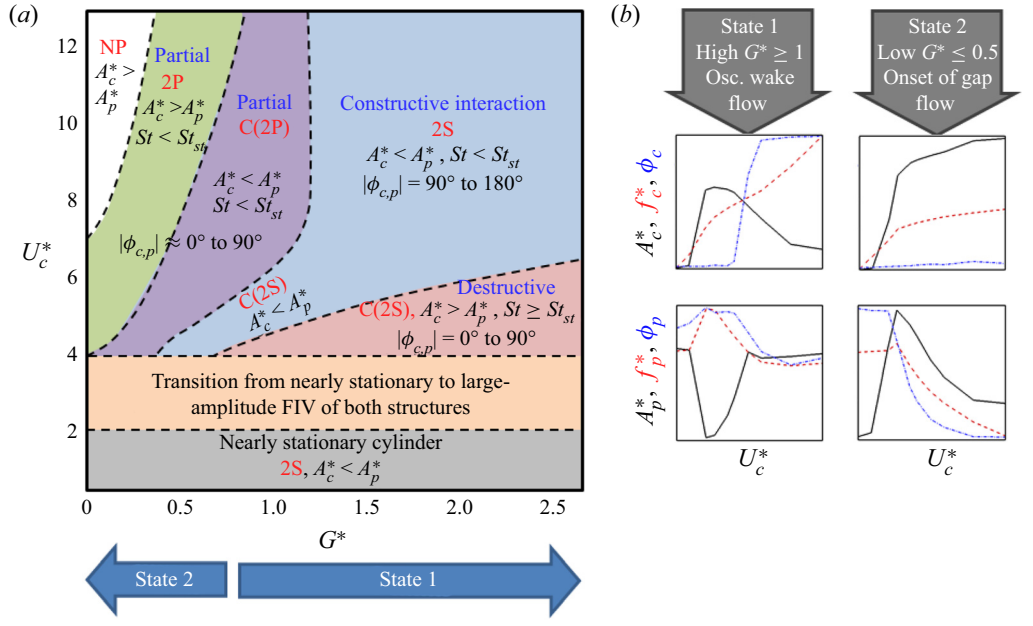

Figure 17. Graphical summary of the proximity-induced flow physics and coupled vibration characteristics of the present multi-physics FMSI system: effect of reduced velocity U_c^* and gap G^* on the two states of the flow behind the cylinder, vortex-interaction regimes in the near wake, vortex-shedding patterns in the far wake, and the representative FICV characteristics of the two structures.

the present FMSI system shows a two-state response, where state 1 occurs at larger gaps ($G^* \geqslant 1$) and state 2 occurs at smaller gaps ($G^* \leqslant 0.5$).

For state 1 at larger gaps $G^* \geqslant 1$, the plate faces the oscillating wake flow. The graphical summary in figure 17 shows the cylinder amplitude A_c^*, frequency ratio f_c^*, and phase difference ϕ_c with a representative rapid increase/gradual decay VIV-like response, continuously increasing, and rapid-jump characteristic, respectively. For the plate, the figure shows a valley–plateau amplitude A_p^* response, summit–plateau frequency f_p^* response, and gradually decreasing phase difference ϕ_p response. These structural responses are associated with a transition in the vortex-interaction mode in the near wake, and the vortex-shedding pattern in the far wake. The figure for state 1 at $G^* \geqslant 1$ shows that the vortex-shedding regime transits from 2S to C(2S) and back to 2S, with increasing U_c^*, for all the gaps except the transition from 2S to C(2S) to C(2P) pattern for $G^* = 1$. The 2S, C(2S) and C(2P) vortex-shedding patterns are observed when the cylinder vortex interacts with a same-signed plate vortex, opposite-signed plate vortex, and sequentially with a same-signed and an opposite-signed plate vortex, called here constructive, destructive and partial vortex interaction, respectively.

For state 2 at smaller gaps $G^* \leqslant 0.5$, there is an onset of gap flow that leads to a transition in the cylinder vibration characteristics, and figure 17 summarizes a rapid-increase plateau amplitude A_c^* response or a galloping response, rapid-increase constant frequency f_c^* response, and a constant value phase ϕ_c response. For the plate, the figure shows a representative summit-like amplitude A_p^* response, gradually decreasing frequency f_p^* and phase difference ϕ_p response with increasing U_c^*. These structural responses are associated with a transition from C(2S) to C(2P) to 2P at $G^* = 0.5$, and

further to a non-periodic mode of vortex shedding at $G^* \leqslant 0.3$ (figure 17). The partial interaction, observed in state 2, results in the formation of a 2P (C(2P)) pattern for a weaker (stronger) cylinder–plate vortex interaction.

The vortex dynamics observed in both the states are also associated with quantitative vibration parameters, where figure 17 shows that the 2S vortex-shedding pattern is observed only when the plate oscillates with a larger amplitude than the cylinder ($A_p^* > A_c^*$), with a low frequency ($St < St_{st}$) and with a phase difference $|\phi_{c,p}| = 90^\circ$ to 180°. As the cylinder amplitude exceeds the plate amplitude in state 1, figure 17 shows a C(2S) pattern with a large oscillation frequency ($St \geqslant St_{st}$) and a phase difference $|\phi_{c,p}| = 0^\circ$ to 90°. However, for $A_c^* > A_p^*$ in state 2, the figure shows a 2P pattern with a small oscillation frequency ($St < St_{st}$) and $|\phi_{c,p}| = 0^\circ$ to 90°. The 2P pattern transits to the 2S pattern at large U_c^* with increasing G^*, with an intermediate C(2P) pattern, which is observed when the two structures oscillate with a low frequency ($St < St_{st}$), with a phase difference $|\phi_{c,p}| = 60^\circ$ to 90° and $A_c^* < A_p^*$. The present demarcations of the vortex-interaction modes and vortex-shedding modes are based on a qualitative observation, which is similar to that adopted in the previous studies Gopalkrishnan *et al.* (1994) for vortex-interaction modes and Williamson & Roshko (1988) for vortex-shedding modes. The present work further reveals certain quantitative parameters – $|\phi_{c,p}|$ for vortex-interaction modes (figure 12), and relative magnitude of A_c^* and A_p^* for vortex-shedding modes (figure 16) – for the demarcation of both the modes, with a few exceptions.

The present work is significant as it presents the role of proximity interference on the flow physics (flow regimes behind the cylinder, cylinder–plate vortex interaction and the associated vortex-shedding patterns) and coupled vibrational characteristics of both the structures. For an energy-harvesting application of the present FMSI problem, a larger vibrational amplitude is desired for both the cylinder and the plate, which is obtained here for intermediate $U_c^* \approx 5 - 7$, and will be explored further in our future work.

Declaration of interests. The authors report no conflict of interest.

Author ORCIDs.
Charu Mittal https://orcid.org/0000-0002-0576-8348;
Atul Sharma https://orcid.org/0000-0001-6500-924X.

References

Akaydin, H.D., Elvin, N. & Andreopoulos, Y. 2010 Energy harvesting from highly unsteady fluid flows using piezoelectric materials. *J. Intell. Mater. Syst. Struct.* **21** (13), 1263–1278.

Allen, J.J. & Smits, A.J. 2001 Energy harvesting eel. *J. Fluids Struct.* **15** (3–4), 629–640.

Apelt, C.J., West, G.S. & Szewczyk, A.A. 1973 The effects of wake splitter plates on the flow past a circular cylinder in the range $10^4 < R < 5 \times 10^4$. *J. Fluid Mech.* **61** (1), 187–198.

Bae, J., *et al.* 2014 Flutter-driven triboelectrification for harvesting wind energy. *Nat. Commun.* **5** (1), 1–9.

Barrero-Gil, A., Alonso, G. & Sanz-Andres, A. 2010 Energy harvesting from transverse galloping. *J. Sound Vib.* **329** (14), 2873–2883.

Bearman, P.W. 2011 Circular cylinder wakes and vortex-induced vibrations. *J. Fluids Struct.* **27** (5–6), 648–658.

Bernitsas, M.M, Raghavan, K., Ben-Simon, Y. & Garcia, E.M.H. 2008 Vivace (vortex induced vibration aquatic clean energy): a new concept in generation of clean and renewable energy from fluid flow. *Trans. ASME J. Offshore Mech. Arctic Engng* **130** (4), 041101.

Blackburn, H.M. & Karniadakis, G.E. 1993 Two-and three-dimensional simulations of vortex-induced vibration or a circular cylinder. In *Proceedings of the 3rd International Offshore and Polar Engineering Conference*. International Society of Offshore and Polar Engineers.

BLEVINS, R.D. 1990 *Flow-Induced Vibration*. Van Nostrand Reinhold.

BOKAIAN, A. & GEOOLA, F. 1984*a* Proximity-induced galloping of two interfering circular cylinders. *J. Fluid Mech.* **146**, 417–449.

BOKAIAN, A. & GEOOLA, F. 1984*b* Wake-induced galloping of two interfering circular cylinders. *J. Fluid Mech.* **146**, 383–415.

BORAZJANI, I. & SOTIROPOULOS, F. 2009 Vortex-induced vibrations of two cylinders in tandem arrangement in the proximity–wake interference region. *J. Fluid Mech.* **621**, 321–364.

GOPALKRISHNAN, R., TRIANTAFYLLOU, M.S., TRIANTAFYLLOU, G.S. & BARRETT, D. 1994 Active vorticity control in a shear flow using a flapping foil. *J. Fluid Mech.* **274**, 1–21.

GRIFFIN, O.M., SKOP, R.A. & RAMBERG, S.E. 1975 The resonant, vortex-excited vibrations of structures and cable systems. In *7th Annual Offshore Technology Conference*, paper no. 2319. OTC.

GUPTA, S., THEKKETHIL, N., AGRAWAL, A., HOURIGAN, K., THOMPSON, M.C. & SHARMA, A. 2021 Body-caudal fin fish-inspired self-propulsion study on burst-and-coast and continuous swimming of a hydrofoil model. *Phys. Fluids* **33** (9), 091905.

HWANG, J.-Y., YANG, K.-S. & SUN, S.-H. 2003 Reduction of flow-induced forces on a circular cylinder using a detached splitter plate. *Phys. Fluids* **15** (8), 2433–2436.

JUNG, H.-J. & LEE, S.-W. 2011 The experimental validation of a new energy harvesting system based on the wake galloping phenomenon. *Smart Mater. Struct.* **20** (5), 055022.

KWON, K. & CHOI, H. 1996 Control of laminar vortex shedding behind a circular cylinder using splitter plates. *Phys. Fluids* **8** (2), 479–486.

LANEVILLE, A. & BRIKA, D. 1999 The fluid and mechanical coupling between two circular cylinders in tandem arrangement. *J. Fluids Struct.* **13** (7–8), 967–986.

LEE, J. & YOU, D. 2013 Study of vortex-shedding-induced vibration of a flexible splitter plate behind a cylinder. *Phys. Fluids* **25** (11), 110811.

LEONTINI, J.S., THOMPSON, M.C. & HOURIGAN, K. 2006 The beginning of branching behaviour of vortex-induced vibration during two-dimensional flow. *J. Fluids Struct.* **22** (6–7), 857–864.

LIANG, S., WANG, J., XU, B., WU, W. & LIN, K. 2018 Vortex-induced vibration and structure instability for a circular cylinder with flexible splitter plates. *J. Wind Engng Ind. Aerodyn.* **174**, 200–209.

MITTAL, C. & SHARMA, A. 2021 Flow-induced vibration of a flexible splitter-plate in the wake of a stationary cylinder. *Phys. Fluids* **33** (11), 113607.

MITTAL, S. & KUMAR, V. 2001 Flow-induced oscillations of two cylinders in tandem and staggered arrangements. *J. Fluids Struct.* **15** (5), 717–736.

PAÏDOUSSIS, M.P., PRICE, S.J. & DE LANGRE, E. 2010 *Fluid-Structure Interactions: Cross-Flow-Induced Instabilities*. Cambridge University Press.

PAPAIOANNOU, G.V., YUE, D.K.P., TRIANTAFYLLOU, M.S. & KARNIADAKIS, G.E. 2008 On the effect of spacing on the vortex-induced vibrations of two tandem cylinders. *J. Fluids Struct.* **24** (6), 833–854.

PFISTER, J.-L. & MARQUET, O. 2020 Fluid–structure stability analyses and nonlinear dynamics of flexible splitter plates interacting with a circular cylinder flow. *J. Fluid Mech.* **896**, A24.

PRASANTH, T.K. & MITTAL, S. 2008 Vortex-induced vibrations of a circular cylinder at low Reynolds numbers. *J. Fluid Mech.* **594**, 463–491.

ROSHKO, A. 1954 On the drag and shedding frequency of two-dimensional bluff bodies. *NACA Tech. Rep.* TN 3169.

ROSTAMI, A.B. & ARMANDEI, M. 2017 Renewable energy harvesting by vortex-induced motions: review and benchmarking of technologies. *Renew. Sust. Energy Rev.* **70**, 193–214.

SAHU, T.R., FURQUAN, M. & MITTAL, S. 2019 Numerical study of flow-induced vibration of a circular cylinder with attached flexible splitter plate at low *Re*. *J. Fluid Mech.* **880**, 551–593.

SARPKAYA, T. 1995 Hydrodynamic damping, flow-induced oscillations, and biharmonic response. *Trans. ASME J. Offshore Mech. Arctic Engng* **117** (4), 232–238.

SARPKAYA, T. 2004 A critical review of the intrinsic nature of vortex-induced vibrations. *J. Fluids Struct.* **19** (4), 389–447.

SERSON, D., MENEGHINI, J.R., CARMO, B.S., VOLPE, E.V. & GIORIA, R.S. 2014 Wake transition in the flow around a circular cylinder with a splitter plate. *J. Fluid Mech.* **755**, 582–602.

SHARMA, A. 2016 *Introduction to Computational Fluid Dynamics: Development, Application and Analysis*. John Wiley & Sons.

SHI, S., NEW, T.H. & LIU, Y. 2013 Flapping dynamics of a low aspect-ratio energy-harvesting membrane immersed in a square cylinder wake. *Exp. Therm. Fluid Sci.* **46**, 151–161.

SHIELS, D., LEONARD, A. & ROSHKO, A. 2001 Flow-induced vibration of a circular cylinder at limiting structural parameters. *J. Fluids Struct.* **15** (1), 3–21.

SHUKLA, S., GOVARDHAN, R.N. & ARAKERI, J.H. 2013 Dynamics of a flexible splitter plate in the wake of a circular cylinder. *J. Fluids Struct.* **41**, 127–134.

TECHET, A.H., ALLEN, J.J. & SMITS, A.J. 2002 Piezoelectric eels for energy harvesting in the ocean. In *Proceedings of the 12th International Offshore and Polar Engineering Conference*, pp. 713–718. ISOPE.

THEKKETHIL, N. & SHARMA, A. 2019 Level set function–based immersed interface method and benchmark solutions for fluid flexible-structure interaction. *Intl J. Numer. Meth. Fluids* **91** (3), 134–157.

THEKKETHIL, N. & SHARMA, A. 2020 Hybrid Lagrangian–Eulerian method-based CFSD development, application, and analysis. In *Immersed Boundary Method* (ed. S. Roy, A. De & E. Balaras), pp. 361–394. Springer.

THEKKETHIL, N., SHARMA, A. & AGRAWAL, A. 2018 Unified hydrodynamics study for various types of fishes-like undulating rigid hydrofoil in a free stream flow. *Phys. Fluids* **30** (7), 077107.

THEKKETHIL, N., SHARMA, A. & AGRAWAL, A. 2020 Self-propulsion of fishes-like undulating hydrofoil: a unified kinematics based unsteady hydrodynamics study. *J. Fluids Struct.* **93**, 102875.

UNAL, M.F. & ROCKWELL, D. 1988 On vortex formation from a cylinder. Part 2. Control by splitter-plate interference. *J. Fluid Mech.* **190**, 513–529.

VILLARREAL, D.J.Y. 2018 Vortex resonance wind turbine. US Patent No. 9856854.

WANG, H., ZHAI, Q. & ZHANG, J. 2018 Numerical study of flow-induced vibration of a flexible plate behind a circular cylinder. *Ocean Engng* **163**, 419–430.

WANG, J., GENG, L., DING, L., ZHU, H. & YURCHENKO, D. 2020 The state-of-the-art review on energy harvesting from flow-induced vibrations. *Appl. Energy* **267**, 114902.

WILLIAMSON, C.H.K. & GOVARDHAN, R. 2004 Vortex-induced vibrations. *Annu. Rev. Fluid Mech.* **36**, 413–455.

WILLIAMSON, C.H.K. & JAUVTIS, N. 2004 A high-amplitude 2T mode of vortex-induced vibration for a light body in XY motion. *Eur. J. Mech. (*B*/Fluids)* **23** (1), 107–114.

WILLIAMSON, C.H.K. & ROSHKO, A. 1988 Vortex formation in the wake of an oscillating cylinder. *J. Fluids Struct.* **2** (4), 355–381.

WU, J., QIU, Y.L., SHU, C. & ZHAO, N. 2014 Flow control of a circular cylinder by using an attached flexible filament. *Phys. Fluids* **26** (10), 103601.

ZDRAVKOVICH, M.M. 1985 Flow induced oscillations of two interfering circular cylinders. *J. Sound Vib.* **101** (4), 511–521.

ZDRAVKOVICH, M.M. & MEDEIROS, E.B. 1991 Effect of damping on interference-induced oscillations of two identical circular cylinders. *J. Wind Engng Ind. Aerodyn.* **38** (2–3), 197–211.

ZHOU, C.Y., SO, R.M.C. & LAM, K. 1999 Vortex-induced vibrations of an elastic circular cylinder. *J. Fluids Struct.* **13** (2), 165–189.

ZIENKIEWICZ, O.C., KELLY, D.W. & BETTESS, P. 1977 The coupling of the finite element method and boundary solution procedures. *Intl J. Numer. Meth. Engng* **11** (2), 355–375.